Research Paper

Title:

Thermodynamic Analysis and Effect of Crystallinity for Silicon Monoxide Negative Electrode for Lithium Ion Batteries

Authors:

Kouji Yasuda,[a,b,*] Yusuke Kashitani,[c] Shingo Kizaki,[c] Kohki Takeshita,[c] Takehisa Fujita,[c] and Shinji Shimosaki[c]

Affiliations:

[a]Environment, Safety and Health Organization, Kyoto University, Yoshida-honmachi, Sakyo-ku, Kyoto 606-8501, Japan

[b]Graduate School of Energy Science, Kyoto University, Yoshida-honmachi, Sakyo-ku, Kyoto 606-8501, Japan

[c]High-Performance Materials Manufacturing Department, OSAKA Titanium technologies Co., Ltd., 1, Higashihama-cho, Amagasaki, Hyogo 660-8533, Japan

Corresponding Author:

*E-mail: yasuda.kouji.3v@kyoto-u.ac.jp (K. Yasuda); Tel: +81-75-753-4817; Fax: +81-75-753-5906

Abstract

The electrochemical behavior of SiO negative electrodes for lithium ion batteries is thermodynamically and experimentally investigated. The analysis of the reaction pathway and the calculation of the reaction potentials during the Li insertion/extraction reactions are carried out by the construction of the ternary phase diagram for the Li–Si–O system. In the initial reaction of Li insertion, metallic Si and lithium silicates are formed above 0.37 V vs. Li/Li^+ as a conversion reaction of the SiO negative electrode. Further Li insertion produces Li–Si alloys as reversible reaction phases. The decomposition of the Li_4SiO_4 phase begins before the formation of the Li–Si alloy is completed. The measured electrode behavior of the SiO negative electrode basically agrees with the thermodynamic calculations, especially at a low reaction rate; deviations can be ascribed to kinetic factors and electrode resistance. The values of over 1898 mA h g^{-1} and 71.0% were obtained for the discharge capacity and the coulombic efficiency, respectively. Furthermore, the overvoltage for an amorphous SiO electrode was smaller than that for a disproportionated SiO electrode into Si and SiO_2 phases.

Highlights

- Thermodynamic analysis of SiO electrodes
- Highest discharge capacity and relatively high coulombic efficiency for SiO anode
- Superior characters of amourphous SiO than disproportionated SiO

Keywords

Silicon monoxide, Thermodynamics, Phase diagram, Lithium ion battery

1. Introduction

Lithium ion batteries (LIBs) are widely utilized as efficient storage devices for mobile systems such as laptop computers and cell phones. The large operational voltage derives from the redox reactions for lithium (Li) species both at the positive and negative electrodes. One major concern surrounding LIBs is the insufficient capacity of the graphite negative electrode in the context of long-distance driving for electric vehicles (EVs) and hybrid electric vehicles (HEVs). The development of alloying-dealloying processes with Li by using alloying materials such as silicon (Si) and tin (Sn) as well as conversion-type materials of metal oxides, nitrides, and phosphides constitutes a crucial task toward achieving large capacities [1–3]. Among the various candidates, silicon monoxide (SiO) is expected to have a high capacity and impressive cyclability by overcoming the drawbacks of a large volume expansion and a large irreversible capacity for alloying materials and conversion-type materials, respectively.

In the Si–oxygen (O) binary system [4], silicon dioxide (SiO_2) is the only stable oxide at ambient pressure and temperature. Silicon oxides with lower oxygen content, SiO_x – where x is the atomic ratio of oxygen with respect to silicon, and falls between 0 (Si) and 2 (SiO_2) – have no stable crystalline structure including SiO [5–11]. Among silicon lower oxides, solid SiO is the only commercially available variety, and is usually manufactured with a vapor deposition technique from the gaseous SiO produced by the reaction of Si and SiO_2 at high temperatures [11–13]. The notable characteristic of solid SiO is its disproportionation into solid nanocrystalline Si particles and solid SiO_2 matrix above ~1123 K [14,15]. The crystallinity of the SiO materials changes with the thermal history during the production processes. Accordingly, both the amorphous and disproportionated varieties of SiO are sometimes referred to as “commercial SiO.”

Nevertheless, it should be emphasized that the characteristics of amorphous SiO and disproportionated SiO are different. For instance, the Si valence states for amorphous SiO are evaluated using X-ray photoelectron spectroscopy (XPS) analysis as Si(0), Si(1+), Si(2+), Si(3+), and Si(4+), depending on the number of bonds coordinated with oxygen; on the other hand, the valence states are evaluated as Si(0) and Si(4+) for disproportionated SiO [16–18].

The characteristics of SiO negative electrodes for LIBs have already been reported by many researchers for the case of both amorphous SiO and disproportionated SiO [19–32]. In addition to SiO negative electrodes, the electrochemical characteristics of (SiO + carbon) composite electrodes [33–44] and SiO_2 electrodes [28, 45–50] have also been reported. Table 1 summarizes the results for the SiO phase (amorphous or disproportionated), the intermediate phase during Li insertion/extraction, the initial charge and discharge capacities, the initial coulombic efficiency, and the analysis methods, where the charge/discharge rates and cut-off voltages are irrelevant.

Table 1 Representative reports on battery and electrode characteristics of the SiO negative electrode.

Author, Ref.	Year	SiO phase	Intermediate phase	Initial charge capacity ($mAh\ g^{-1}$)	Initial discharge capacity ($mAh\ g^{-1}$)	Initial coulombic efficiency (%)	Note
Yang et al. [19]	2002	Amor.	-	ca. 2250	ca. 1300	ca. 57.8	-
Nagao et al. [20]	2004	Amor.	SiO_2	1594	-	-	Neutron elastic scattering
Miyachi et al. [21]	2005	Amor.	Li–Si–O, Li_2O	2404	598	24.9	XPS
Miyachi et al. [22]	2007	-	Li–Si–O, Li_2O	2520	1260	50.0	Metal-doped SiO, XPS
Kim et al. [23]	2007	-	Li–Si–O, Li_2O	2680	1470	54.9	NMR, HR-TEM, electrochemical dilatometry. Plateau at 0.8 V vs. Li^+/Li in 1st discharge
Yamada et al. [24]	2007	-	-	-	-	-	Kinetics evaluation by AC impedance spectroscopy
Park et al [25]	2010	Amor./ dispro.	SiO_x	2216/ 185	1104/ 94	49.8/ 50.8	TEM, Disproportionated at 800, 1000, and 1200 ℃.
Komaba et al [26]	2011	-	-	ca. 1800	826	45.9	-
Kim et al., [27]	2011	Amor./ dispro.	Li–Si–O, Li_2O	2410	1300	53.9	NMR, HR-TEM, Differential capacity peaks at 0.08 and 0.24 V vs. Li^+/Li
Yamamura et al. [28]	2011	Dispro.	Li–Si–O	2548	1791	70.3	Plateau at 0.2 and 0.5 V vs. Li^+/Li in 1st discharge. First principles calculation. SiO_2 was also reacted.
Miyuki et al. [29]	2011	Amor./ dispro.	-	-	-	-	$LiFePO_4$/SiO full cell.
Jeong et al. [30]	2012	Dispro.	-	1757	1265	72.0	TiO_2 coated SiO
Kim et al. [31]	2013	Dispro.	-	1958	1413	72.2	Carbon coated SiO. Differential capacity peaks at 0.06, 0.21, 0.31 and 0.48 V vs. Li^+/Li after 5th cycle
Takezawa et al. [32]	2013	Amor.	Li–Si–O, Li_2O	2418	1306	54.0	SiO_x ($0.17 < x < 1.34$) was used. XPS

-: Not given

In this paper, we use the phrases "charge" and "discharge" for Li insertion and extraction reactions, respectively. The Li insertion reaction is reported to proceed with the formation of Li–Si alloys, lithium silicates (Li–Si–O), and/or Li_2O [21,33,34]; moreover, the alloying-dealloying of Si contributes to the reversible capacity. Whereas the formed silicates and Li_2O lead to the irreversible capacity, the silicates play the role of a matrix of nano Si (2–10 nm diameter) for the fast diffusion of Li atoms and the mitigation of structural collapse [24]. The formation of these oxide phases has been evaluated by various techniques such as XPS, nuclear magnetic resonance (NMR), high-resolution transmission electron microscopy (HR-TEM), and electrochemical dilatometry.

The theoretical reaction of a SiO negative electrode was reported as follows [28, 29,51]:

$$20\ SiO + 86\ Li \rightarrow 3\ Li_{22}Si_5 + 5\ Li_4SiO_4. \quad (1)$$

According to Eq. (1), the initial charge and discharge capacities and initial coulombic efficiency are theoretically calculated as 2615 mA h g^{-1}, 2007 mA h g^{-1}, and 76.7%, respectively. However, as understood from Table 1, the reported values for SiO negative electrodes differ among researchers. In addition, the reaction potentials observed as potential plateaus in the potential-charge curves and capacity peaks in voltammograms also differ between reports [34,52]. Consequently, the nature of the electrochemical characteristics of SiO has not yet been sufficiently clarified. Although Yang et al. have provided a thermodynamic analysis of the reaction potentials of a SiO electrode [53], their calculations are not entirely reliable because they do not take into account the Gibbs phase rule that is indispensable for the evaluation of the equilibrium.

In this paper, the reactions for a SiO negative electrode are thermodynamically evaluated. Firstly, the Li–Si–O system is investigated on the basis of the construction of the ternary phase diagram according to the Gibbs phase rule, in which the number of degrees of freedom at a fixed temperature can be expressed as:

$$f = C - P + 1, \quad (2)$$

where f stands for the number of degrees of freedom, C is the number of components, and P is the number of equilibrated phases. Secondly, the formation potentials of Li–Si alloys, lithium silicates, and Li_2O are calculated, and equilibrium potential curves for charge/discharge reactions are drawn. Thirdly, the key factors for high capacity and impressive cycle performance are discussed. Finally, the differences for the charge/discharge behaviors between amorphous SiO and disproportionated SiO are experimentally evaluated.

2. Thermodynamic calculations

Because a SiO electrode is composed of three elements (i.e., Li, Si, and O) during the electrochemical insertion/extraction of Li, the solid electrode can be treated as a material in the Li–Si–O system. From the standpoint of thermochemistry, the stability and behavior of the electrode can be investigated from the ternary phase diagram. However, the diagram for the Li–Si–O system has only been reported at high temperatures above 600 K with the aim of the production of ceramics [54,55], and there has been no report at room temperature. Accordingly, in this section the ternary phase

diagram is constructed at 298 K from the reported thermodynamic data of the compounds. Furthermore, the phase change and equilibrium potentials in the Li insertion/extraction reactions for a SiO negative electrode are analyzed. Against this background, the dependence of battery performance on charge/discharge conditions is discussed.

2-1. Construction of the ternary phase diagram for the Li–Si–O system

In the Li–Si–O system at 298 K, the compounds including solid Li, solid Si, and O_2 gas (listed in Table 2) exist. Only solid Li_2O and SiO_2 are the stable phases in the binary systems for the Li–O [4,56] and Si–O [4,57,58] systems, respectively. According to the quasi-binary phase diagrams for the Li_2O–SiO_2 system [59–61], solid $Li_2Si_2O_5$, Li_2SiO_3, and Li_4SiO_4 are stable phases among the lithium silicates. In the Li–Si system, four compounds ($Li_{12}Si_7$, Li_7Si_3, $Li_{13}Si_4$, and $Li_{22}Si_5$) are reported [62]. These diagrams indicate a negligible composition range for these compounds deriving from the vacancy and solubility.

The thermodynamic data for these compounds in the Li–Si–O system (acquired from the thermodynamic software HSC Chemistry® ver. 5.1 [63]) are also listed in Table 2 [64–72]. Because SiO has no stable crystalline phase at ambient temperature and pressure, its data are not reported. Concerning the thermodynamic data for the Li–Si compounds, there were several reports that used electromotive force (emf) measurements [73–77]. Their data were recalculated by Demidov et al. [78] and Braga et al. [79] using two assessment methods, which were adopted and updated for the construction of the current phase diagram for the Li–Si system [62], respectively. In this study, the standard Gibbs energies of formation at 298 K in the first assessment method in the report by Braga et al. [79] were applied. The phase diagram was constructed by Chesta ver. 2.22,

which is a free software supplied by Kyoto University for creating chemical potential diagrams for multi-component systems [80].

Table 2 Thermodynamic data for Li–Si–O system at 298 K used for the calculation.

Compound				Standard Gibbs energy, G° / kJ mol^{-1}	Standard Gibbs energy of formation, ΔG_f° / kJ mol^{-1}	Ref
Formula	Component					
	Li	Si	O			
Li	1	0	0	–8.7	0	[64–66]
Si	0	1	0	–5.6	0	[67]
O_2	0	0	2	–61.1	0	[66,68]
$Li_{12}Si_7$	12	7	0	–570.5	–426.9	Calculated from [79].
Li_7Si_3	7	3	0	–312.7	–235.0	
$Li_{13}Si_4$	13	4	0	–525.6	–390.1	
$Li_{22}Si_5$	22	5	0	–758.8	–539.4	
Li_2O	2	0	1	–609.1	–561.2	[64,69,70]
SiO_2	0	1	2	–923.2	–856.5	[71]
$Li_2Si_2O_5$	2	2	5	–2598.3	–2416.9	[64]
Li_2SiO_3	2	1	3	–1673.4	–1558.8	[67]
Li_4SiO_4	4	1	4	–2366.2	–2203.6	[72]

Figure 1(a) shows the ternary phase diagram for the Li–Si–O system at 298 K calculated from the reported thermodynamic data in Table 2. As can be seen, the large triangle consists of Li, Si, and 1/2 O_2 vertices; the diagram is divided into small triangles, except for the upper part. According to the Gibbs phase rule at a fixed temperature indicated by Eq. (2) and the value of C = 3 (Li, Si, and O) in the system, three condensed phases indicated as the vertices are equilibrated (f = 0, P = 4 by three phases and gas). On the other hand, at the upper part of the diagram, the triangle of Li_2O–SiO_2–O_2 is not divided into small triangles. In the Li_2O–SiO_2–O_2 system, the value of P is 3 because two condensed phases and the gas phase exist. Thus, the value of f = 1 indicates that the system has one variable, such as the partial pressure of oxygen (p_{O_2}).

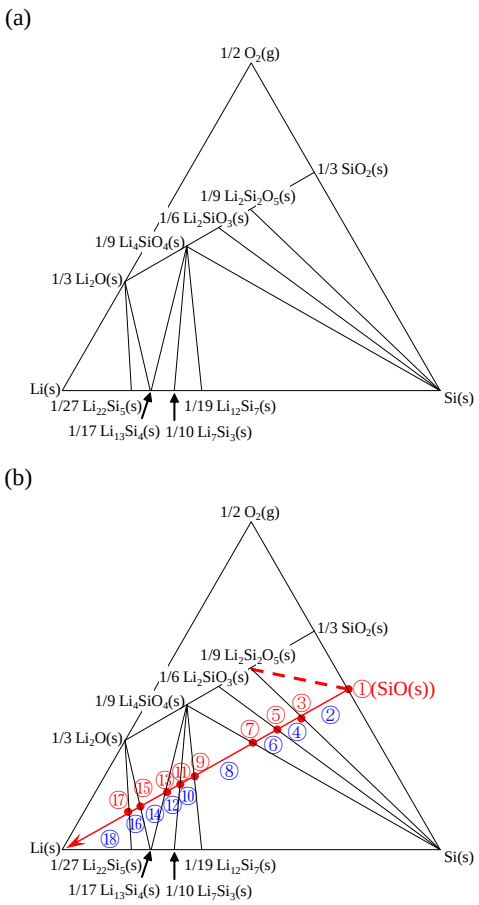

Fig. 1 (a) Calculated ternary phase diagram for the Li–Si–O system at 298 K. (b) Transition of formed phases during the Li insertion for a SiO negative electrode at 298 K shown in the ternary phase diagram for Li–Si–O system.

2-2. Phase change and equilibrium potential for a SiO electrode

Because the position in the ternary phase diagram indicates the nominal composition of the system, the phase change during the electrochemical Li insertion/extraction reaction of a SiO electrode can be discussed based on the equilibrium phases. Assuming that there are no ionic species containing Si and O related to the electrode reactions, the electrode potential, *E*, with respect to the standard potential of Li is a function of the Li activity in the electrode:

$$Li^+ + e^- \rightarrow Li, \quad (3)$$

$$E = \frac{RT}{F} \ln \frac{a_{\mathrm{Li}}}{a_{\mathrm{Li}^+}} = \frac{2.303RT}{F} \log a_{\mathrm{Li}}, \quad (4)$$

where R is the gas constant, T is the absolute temperature, F is the Faraday constant, and a_{Li} and a_{Li^+} are the activities of Li and Li^+ ions, respectively. Here, the standard states of Li and Li^+ ions are pure solid Li and ion concentration dispersed in the electrolyte, respectively. It should be mentioned that the calculation is based on the following assumptions, which are inherent to the discussion of chemical equilibria: the composition of the electrode is homogeneous; the compounds are electrochemically active with Li; and the electrode potential is determined by the activity of Li in the electrode, as expressed by Eq. (4). Another assumption is that the chemical potentials of Si and O_2 in the SiO phase are the same at the equilibrium of Si and SiO_2. The three phases at the vertices are equilibrated when a nominal composition is located within the triangle. The electrode potential takes on a fixed value when the system has zero degrees of freedom according to Eq. (2). Another equilibrium is a two-phase equilibrium whose composition is positioned along a line. The two phases at the side ends are equilibrated with one degree of freedom (f = 1) – i.e., the electrode potential changes.

When the Li insertion reaction occurs for a SiO electrode, the change of nominal composition is expressed as the red arrow drawn from SiO to Li in Fig. 1(b). The calculation suggests the formation of $Li_2Si_2O_5$/Si/SiO_2 in the initial reaction of SiO. In the actual reaction, SiO_2 is not formed and $Li_2Si_2O_5$/SiO/Si are equilibrated as the red broken line becomes a side of the triangle.

The formation of Li–Si–O compounds ($Li_aSi_bO_c$, where a, b, and c are stoichiometric ratios) from metallic Li and Si as well as O_2 gas at atmospheric pressure can be expressed as follows:

$$a\ \mathrm{Li} + b\ \mathrm{Si} + \mathrm{c/2}\ \mathrm{O_2} = \mathrm{Li}_a\mathrm{Si}_b\mathrm{O}_c. \quad (5)$$

The chemical potentials of Li, Si, and O_2 can be expressed as a function of the standard Gibbs energy of formation of $\mathrm{Li}_a\mathrm{Si}_b\mathrm{O}_c$ ($\Delta G_\mathrm{f}^\circ(\mathrm{Li}_a\mathrm{Si}_b\mathrm{O}_c)$):

$$a\,(G^\circ(\mathrm{Li}) + RT\ln a_{\mathrm{Li}}) + b\,(G^\circ(\mathrm{Si}) + RT\ln a_{\mathrm{Si}}) + c/2\,(G^\circ(\mathrm{O_2}) + RT\ln p_{\mathrm{O_2}})$$
$$= G^\circ(\mathrm{Li}_a\mathrm{Si}_b\mathrm{O}_c), \quad (6)$$

$$2.303RT\,(a\log a_{\mathrm{Li}} + b\log a_{\mathrm{Si}} + c/2\log p_{\mathrm{O_2}})$$
$$= G^\circ(\mathrm{Li}_a\mathrm{Si}_b\mathrm{O}_c) - (aG^\circ(\mathrm{Li}) + bG^\circ(\mathrm{Si}) + \mathrm{c/2}\,G^\circ(\mathrm{O_2}))$$
$$= \Delta G_\mathrm{f}^\circ(\mathrm{Li}_a\mathrm{Si}_b\mathrm{O}_c). \quad (7)$$

Here, $G^\circ(\mathrm{Li})$, $G^\circ(\mathrm{Si})$, and $G^\circ(\mathrm{O_2})$ are the standard Gibbs energy of Li, Si, and O_2, respectively, and a_{Si} is the activity of Si with respect to pure solid Si.

As shown in Eq. (7), a_{Li}, a_{Si}, and $p_{\mathrm{O_2}}$ are variables under the existence of a single phase only. On the other hand, they take on fixed values at the equilibrium state of three phases where the standard Gibbs energies of these compounds simultaneously satisfy Eq. (7). By combining the two compounds, the chemical potentials at the $Li_2Si_2O_5$/Si/SiO_2 equilibrium (region ② in Fig. 1(b)) can be calculated in Eq. (8):

$$2.303RT\begin{pmatrix} 2 & 2 & \frac{5}{2} \\ 0 & 1 & 0 \\ 0 & 1 & 1 \end{pmatrix}\begin{pmatrix} \log a_{\mathrm{Li}} \\ \log a_{\mathrm{Si}} \\ \log p_{\mathrm{O_2}} \end{pmatrix} = \begin{pmatrix} \Delta G_{\mathrm{f}}^{\circ}(\mathrm{Li_2Si_2O_5}) \\ \Delta G_{\mathrm{f}}^{\circ}(\mathrm{Si}) \\ \Delta G_{\mathrm{f}}^{\circ}(\mathrm{SiO_2}) \end{pmatrix}. \quad (8)$$

Namely, log a_{Li}, log a_{Si}, and log $p_{\mathrm{O_2}}$ are calculated by Eq. (9) as −24.2, 0, and −150.1, respectively, from the values of ΔG_f° for $Li_2Si_2O_5$, Si, and SiO_2 listed in Table 2. The electrode potential at this equilibrium is obtained to be 1.428 V vs. Li/Li^+ by Eq. (4).

With the progress of Li insertion, the nominal composition reaches the $Li_2Si_2O_5$/Si two-phase equilibrium (point ③). The potential shifts to a negative value during the two-phase equilibrium. Further Li insertion introduces the reaction state of the $Li_2Si_2O_5$/Li_2SiO_3/Si equilibrium (region ④). The chemical potentials and electrode potential can be calculated in the same manner as in the previous paragraph using Eqs. (4) and (8). At the end, the system reaches the Li/Li_2O/$Li_{22}Si_5$ equilibrium (region ⑱). The equilibrium phases and electrode potentials during the Li insertion of a SiO electrode are summarized in Table 3.

Table 3 Equilibrium phases and electrode potentials during the Li insertion for a SiO negative electrode at 298 K.

	Equilibrium phases			Activity or pressure				Equilibrium potential, E, / V (vs. Li^+/Li)
				$\log p_{O2}$	$\log a_{Si}$	$\log a_{Li}$	a_{Li}	
①	Si	SiO_2						
②	Si	SiO_2	$Li_2Si_2O_5$	–150.1	0	–24.2	6.9×10^{-25}	1.428
③	Si	$Li_2Si_2O_5$						↓
④	Si	$Li_2Si_2O_5$	Li_2SiO_3	–150.4	0	–23.8	1.6×10^{-24}	1.406
⑤	Si	Li_2SiO_3						↓
⑥	Si	Li_2SiO_3	Li_4SiO_4	–160.2	0	–16.5	3.4×10^{-17}	0.973
⑦	Si	Li_4SiO_4						↓
⑧	Si	$Li_{12}Si_7$	Li_4SiO_4	–180.6	0	–6.24	5.8×10^{-17}	0.368
⑨	$Li_{12}Si_7$	Li_4SiO_4						↓
⑩	$Li_{12}Si_7$	Li_7Si_3	Li_4SiO_4	–182.1	–2.27	–4.91	1.2×10^{-5}	0.290
⑪	Li_7Si_3	Li_4SiO_4						↓
⑫	Li_7Si_3	$Li_{13}Si_4$	Li_4SiO_4	–183.2	–5.17	–3.67	2.1×10^{-4}	0.217
⑬	$Li_{13}Si_4$	Li_4SiO_4						↓
⑭	$Li_{13}Si_4$	Li_4SiO_4	Li_2O	–183.3	–6.21	–3.35	4.5×10^{-4}	0.198
⑮	$Li_{13}Si_4$	Li_2O						↓
⑯	$Li_{13}Si_4$	$Li_{22}Si_5$	Li_2O	–190.4	–12.0	–1.58	2.7×10^{-2}	0.093
⑰	$Li_{22}Si_5$	Li_2O						↓
⑱	$Li_{22}Si_5$	Li_2O	Li	–196.7	–18.9	0	1	0

Figure 1(b) provides information on the reaction pathway for a SiO electrode. The reaction can be divided into three stages. (1) At the initial stage of the reaction, lithium silicates ($Li_2Si_2O_5$, Li_2SiO_3, and Li_4SiO_4) are formed together with metallic Si (from point ① to point ⑦). (2) Secondly, the formed metallic Si reacts with Li to form Li–Si alloys ($Li_{12}Si_7$, Li_7Si_3, and $Li_{13}Si_4$) that are in equilibrium with Li_4SiO_4 (from point ⑦ to point ⑬). (3) Thirdly, Li_4SiO_4 is decomposed to form Li_2O and $Li_{13}Si_4$. (4) Further Li insertion produces $Li_{22}Si_5$ from $Li_{13}Si_4$ (from point ⑮ to point ⑰). (5) Finally, metallic Li is deposited (after point ⑱). Steps (1) and (2) proceed in accordance with the various reports on the formation of Li–Si alloys in a lithium silicate matrix [21,33,34].

The calculated phase diagram also explains two other reactions. One is the electrochemical reaction of a SiO_2 electrode with Li. In spite of the strong insulating

characteristics of SiO_2, the Li insertion reaction forms lithium silicates in the initial stage in the same manner as the SiO electrode; from this point the alloying reaction of Si demonstrates a reversible capacity, as shown in Fig. 2(a). The formation of lithium silicates agrees with the previous reports [28,46–48,50]. The other reaction is the electrochemical inactiveness of Li_4SiO_4 as reported in Ref. [28], in which no Li dissolution reaction occurs for Li_4SiO_4, even at the positive potential of 4.0 V vs. Li/Li^+. As shown in Fig. 2(b), the Li extraction reaction of Li_4SiO_4 leads to the formation of O_2 gas and other silicates with low Li concentration.

$$Li_4SiO_4 \rightarrow Li_2SiO_3 + 1/2\ O_2 + 2\ Li^+ + 2\ e^-. \quad (9)$$

Therefore, Li_4SiO_4 is expected to be stable even at very positive potentials and until the reaction of O_2 gas evolution (reaction (9)). The high stability of lithium silicates suggests that their formation takes on an irreversible capacity, which enables the stable charge/discharge reactions as a matrix of nano crystals of Li–Si alloys. Namely, the electrode acts as a mixture of irreversible Li_4SiO_4 and reversible Li–Si alloys.

$$Li_{13}Si_4 \rightleftarrows 4\ Si + 13\ Li^+ + 13\ e^-. \quad (10)$$

According to the previous reports [28,29,51], the alloy formation instead of the composition of $Li_{22}Si_5$ proceeds as a reversible reaction.

$$Li_{22}Si_5 \rightleftarrows 5\ Si + 22\ Li^+ + 22\ e^-. \quad (11)$$

On the other hand, the thermodynamic calculations suggest that the reversible reaction occurs between Si and $Li_{13}Si_4$ with the Li_4SiO_4 matrix. When alloying reaction is utilized for $Li_{22}Si_5$ composition, the decomposition of Li_4SiO_4 and formation of Li_2O are inevitable.

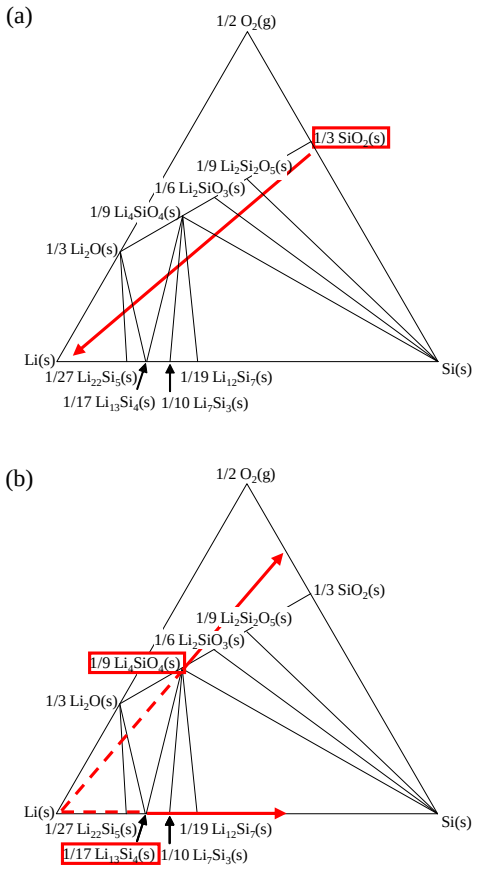

Fig. 2 Reaction pathway during (a) the Li insertion for a SiO_2 negative electrode and (b) the Li desertion for a Li_4SiO_4 electrode at 298 K shown in the ternary phase diagram for Li–Si–O system.

According to the calculated potentials in Table 3, the theoretical potential shift during the Li insertion reaction for a SiO electrode (with equilibrium maintained) is shown in Fig. 3(a). In practice, because the reaction does not proceed at equilibrium states, a similar shift can be obtained at an extremely slow charge rate. As explained

above, the electrode potential remains fixed at the three-phase equilibrium, which is represented by the inside of the triangles according to the Gibbs phase rule. By way of contrast, the potential changes at the two-phase equilibrium, which is represented by the sides of the triangles. In the Li insertion reaction, the potential plateaus corresponding to the formation of lithium silicates are initially observed around 1.4 V (point ②–④) and 1.0 V (⑥) vs. Li/Li^+ with a capacity of 608 mA h g^{-1}. At this stage, the formation of Li–Si alloys starts at 0.37 V (⑧) and continues until 0.22 V (⑫) with a capacity of 1482 mA h g^{-1}. At state ⑭, the Li_4SiO_4 phase is decomposed into Li_2O and $Li_{13}Si_4$. Then, the Li–Si alloy formation is finalized with the composition of $Li_{22}Si_5$ (point ⑰).

The relationship among the amount of inserted Li, the charge capacity, and the reaction equation is theoretically summarized in Table 4. In the practical electrode, SEI (solid-electrolyte interface) formation can also occur, especially at negative potentials. In Ref. [23], the potential plateau at 0.8 V in the initial charge was ascribed to SEI formation. The calculated potential shift in Fig. 3 strongly suggests that the plateau corresponds to the formation of lithium silicates, as well as the deviation due to the overvoltage for the reaction and the ohmic drop. Electrode behaviors reported by other researchers, such as the differential capacity peaks [27,31], can be also explained by the theoretical potential of as lithium silicate formation at 1.4 V and 1.0 V.

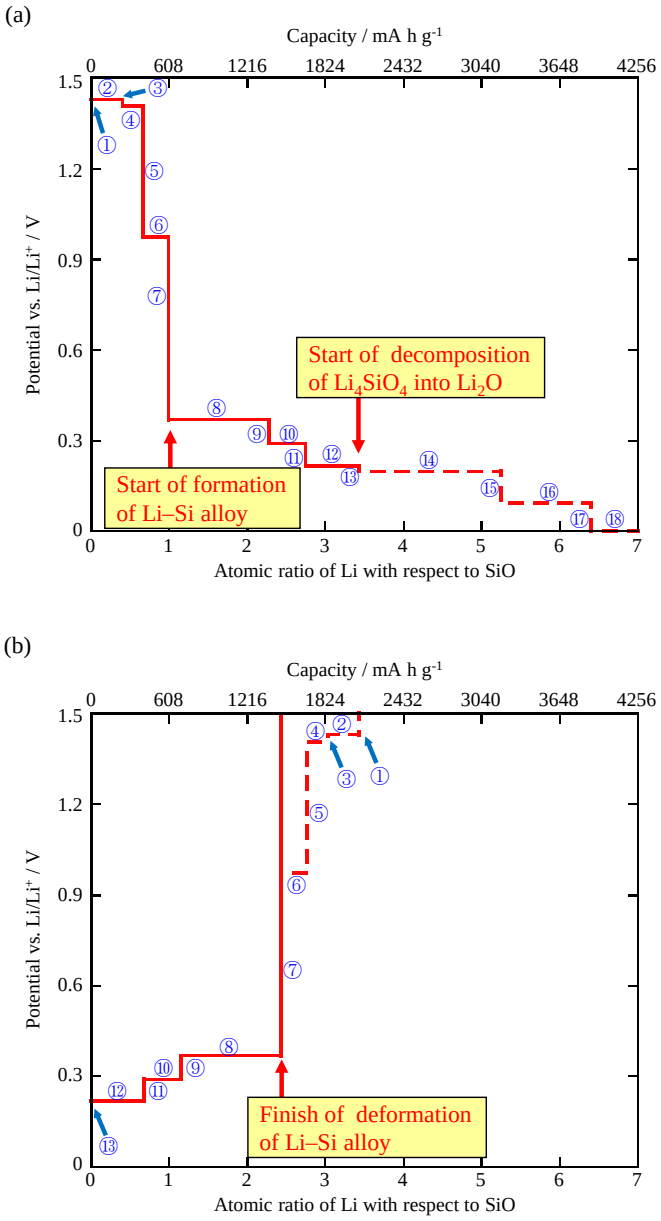

Fig. 3 Transition of equilibrium electrode potential during the Li (a) insertion and (b) desertion after the formation of $Li_{13}Si_4$ for a SiO negative electrode at 298 K shown in the ternary phase diagram for Li–Si–O system.

Figure 3(b) shows the equilibrium potential during the Li extraction reaction for a SiO electrode, which occurs after Li insertion and continues until the completion of the $Li_{13}Si_4$ formation (point ⑬). A reversible capacity of 1482 mA h g^{-1} with 70.9% coulombic efficiency from the Li–Si alloys appears until the reaction reaches the

formation of Si and Li_4SiO_4 (point ⑦). Further Li insertion indicated by the broken line does not occur because Li_4SiO_4 is inactive, as reported in Ref. [28]. When Li insertion further proceeds to form Li_2O, the discharge capacity and coulombic efficiency increase in spite of the decomposition of Li_4SiO_4 (until points ⑮ and ⑰). The amount of extracted Li, the discharge capacity, and the coulombic efficiency corresponding to each reaction are listed in Table 5.

Table 4 The calculated reactions for the Li insertion of a SiO negative electrode at 298 K.

	Reaction	Atomic ratio of Li with respect to SiO	Charge capacity, C_c / mA h g^{-1}
③	$5SiO + 2Li^+ + 2e^- \rightarrow 3Si + Li_2Si_2O_5$	0.40	243
⑤	$3SiO + 2Li^+ + 2e^- \rightarrow 2Si + Li_2SiO_3$	0.67	405
⑦	$4SiO + 4Li^+ + 4e^- \rightarrow 3Si + Li_4SiO_4$	1.00	608
⑨	$28SiO + 64Li^+ + 64e^- \rightarrow 3Li_{12}Si_7 + 7Li_4SiO_4$	2.29	1390
⑪	$12SiO + 33Li^+ + 33e^- \rightarrow 3Li_7Si_3 + 3Li_4SiO_4$	2.75	1672
⑬	$16SiO + 55Li^+ + 55e^- \rightarrow 3Li_{13}Si_4 + 4Li_4SiO_4$	3.44	2090
⑮	$4SiO + 21Li^+ + 21e^- \rightarrow Li_{13}Si_4 + 4Li_2O$	5.25	3192
⑰	$5SiO + 32Li^+ + 32e^- \rightarrow Li_{22}Si_5 + 5Li_2O$	6.40	3891

Table 5 The calculated reactions for the Li extraction of a SiO negative electrode at 298 K.

Charged state	Dis-charged state	Reaction	Atomic ratio of Li with respect to SiO	Discharge capacity, C_d / mA h g^{-1}	Coulombic efficiency (%)
⑬	⑪	$3Li_{13}Si_4 + 4Li_4SiO_4 \rightarrow 4Li_7Si_3 + 4Li_4SiO_4 + 11Li^+ + 11e^-$	0.69	418	20.0
	⑨	$21Li_{13}Si_4 + 28Li_4SiO_4 \rightarrow 12Li_{12}Si_7 + 28Li_4SiO_4 + 129Li^+ + 129e^-$	1.15	700	33.5
	⑦	$3Li_{13}Si_4 + 4Li_4SiO_4 \rightarrow 12Si + 4Li_4SiO_4 + 39Li^+ + 39e^-$	2.44	1482	70.9
⑮		$Li_{13}Si_4 + 4Li_2O \rightarrow 3Si + Li_4SiO_4 + 17Li^+ + 17e^-$	4.25	2584	81.0
⑰		$4Li_{22}Si_5 + 20Li_2O \rightarrow 15Si + 5Li_4SiO_4 + 108Li^+ + 108e^-$	5.40	3283	84.4

2-3. Relationship between the charge/discharge conditions and performances for SiO electrodes

On the basis of the ternary phase diagram for the Li–Si–O system at 298 K (Fig. 1) and the theoretical potential shift during the Li insertion/extraction reaction for a SiO electrode (Fig. 3), the optimum conditions and the key factors for high capacity and impressive cycle performance herein discussed.

The analysis of the previous reports listed in Table 1 indicates that the initial discharge capacity is not necessarily dependent on the initial charge capacity. For example, a discharge capacity of around 1300 mA h g^{-1} is obtained even at charge capacities of 1750 mA h g^{-1} [30] and 2200–2500 mA h g^{-1} [19,22,27,32]. Furthermore, a discharge capacity of 1450 mA h g^{-1} is obtained at charge capacities of 1950 mA h g^{-1} [31] and 2700 mA h g^{-1} [23]. Naturally, the initial coulombic efficiency is different between the reports. Table 1 also clarifies that Li_2O is formed as the intermediate phase in the reports of the higher charge capacity in addition to the lithium silicates [22,23,27,32].

The fact that the initial discharge capacity is not necessarily dependent on the initial charge capacity also explains the effects of Li_2O formation on discharge capacity. Whereas different initial discharge capacities are obtained as 1300 [22,27,32] and 1800 mA h g^{-1} [28] even at the initial capacity around 2500 mA h g^{-1}, the discharge capacity remains low in case of Li_2O formation. However, according to Table 4, the atomic ratio of Li/SiO corresponding to $Li_{13}Si_4$ alloy formation is higher for Li_2O (i.e., 5.25) than for Li_4SiO_4 (i.e., 3.44). These values suggest that the discharge capacity after the charge and until Li_2O formation has a theoretically higher value, and indicates the degraded kinetics for Li_2O formation and/or lithium silicate decomposition while some research on Li conduction for Li_2O has been investigated [81]. The matrix roles of lithium silicates for Li conduction, expansion, relaxation, and electric contact are the key factors for high performance.

Consequently, the combination of the performance reported in the literature and the calculated ternary phase diagram indicates that the crucial charge/discharge condition consists of avoiding or minimizing the formation of Li_2O, which induces two negative effects concerning the low utilization of the inserted Li and the poor reaction kinetics.

3. Experimental

Amorphous SiO powder (Osaka Titanium technologies) with a mean diameter of D_{50} = 4.8 μm was used. The preparation of disproportionated SiO powder was carried out by the thermal treatment of amorphous SiO powder. Amorphous SiO powder contained in an alumina crucible was placed in an Ar atmosphere in an electric furnace maintained at 1273 K or 1473 K for 5 h. As shown in the transmission electron microscope (TEM) images (JEOL, JEM-ARM200F) and X-ray diffraction (XRD) patterns (PANalytical, X'Pert Powder) in Fig. 4, Si nano clusters with a diameter smaller than 10 nm were formed in the SiO_2 matrix by the disproportionation of amorphous SiO.

For the preparation of SiO working electrodes, SiO powder (80 wt%) and Ketjen black (KB) as a conductive additive (5 wt%) were thoroughly mixed with polyimide (PI) as a binder (15 wt%). A slurry was prepared by adding N-methylpyrrolidinone as a solvent to the mixture. For comparison, a slurry consisted of 25wt%-KB and 75wt%-PI was also prepared. The obtained slurry was cast onto a sheet of copper foil, and predried at 393 K in air to remove the solvent. The electrodes were obtained after a final dry at 623 K under a vacuum for 1 h in an electric furnace. The loading mass density fell in the range of 3.5–4.5 mg cm^{-2}. The SiO electrode was prepared by stamping the copper foil into a circle with an area of 1 cm^2. Two-electrode 2032-type coin cells – with the SiO and lithium metal as working and counter electrodes, respectively – were assembled in an Ar

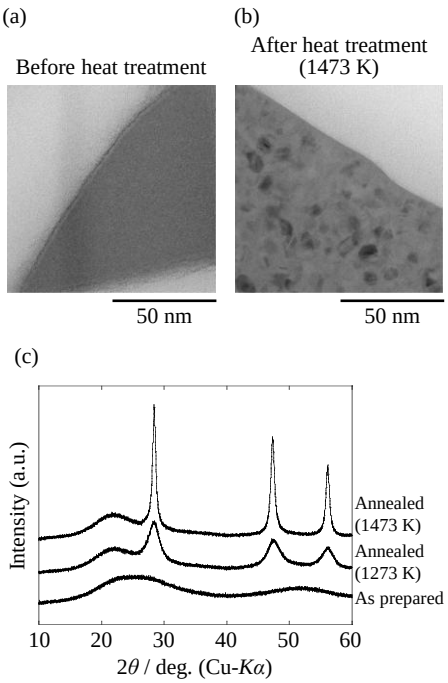

Fig. 4 (a, b) TEM images and (c) XRD patterns for the silicon monoxide particles before and after the heat treatment in an Ar atmosphere at 1273 K and 1473 K.

glovebox. Ethylene carbonate (EC)/diethyl carbonate (DEC) (1:1 by volume) with the addition of 1 mol L^{-1} $LiPF_6$ was used as an electrolyte. The separator was made of polypropylene (PP). The SiO/EC:DEC(1:1) + 1 mol L^{-1} $LiPF_6$/Li cells were operated for charge/discharge reactions.

The formation potentials of the related species were evaluated at a slow rate reaction under the constant current (CC) mode at 15 mA g^{-1} until a voltage of 0 V (charge), and at 15 mA g^{-1} until a voltage of 1.5 V (discharge). The cell performance was evaluated under the constant-current/constant-voltage (CC-CV) mode in the voltage range of 0.005–1.5 V at 298 K. The constant-current/constant-voltage mode was used in order to investigate the lifetime of SiO material under the minimization of the overpotential and ormic drop. During the 1st cycle, the charge conditions were a CC of 150 mA g^{-1} until a voltage of 0.005 V, and a CV of 0.005 V until a current of 15 mA g^{-1}; discharge conditions were a

CC of 150 mA g^{-1} until a voltage of 1.5 V. During the 2nd cycle, the charge conditions were a CC of 450 mA g^{-1} until a voltage of 0.005 V, and a CV of 0.005 V until a current of 15 mA g^{-1}; discharge conditions were a CC of 450 mA g^{-1} until a voltage of 1.5 V. After the 3rd cycle, the charge conditions were a CC of 750 mA g^{-1} until a voltage of 0.005 V, and a CV of 0.005 V until a current of 15 mA g^{-1}; discharge conditions were a CC of 750 mA g^{-1} until a voltage of 1.5 V.

4. Results and discussion

4-1. Confirmation of formation potentials

The analysis of the electrochemical reaction can be carried out by separating it into equilibrium and kinetic factors. As the first component of the experimental, the electrode behavior was examined at a low charge rate in order to minimize the kinetic factor.

Figure 5(a) shows the equilibrium potential shift until the end of the Li–Si alloy formation with the charge/discharge curves of (SiO + KB + PI) anode recorded at a rate of 15 mA g^{-1}, which is slower than a 0.01 C rate. For comparison, the curves of (25wt% KB + 75wt% PI) are shown in Fig. 5(b). The rate was 10 mA g^{-1}, which was also as large as a 0.01 C rate. Clearly, a potential plateau is observed until 600 mA h g^{-1} at 0.35–0.5 V for the curve of amorphous SiO (Fig. 5(a)). Almost the same capacity of 600 mA h g^{-1} with the theoretical value indicates that the plateau corresponds to the formation of lithium silicate. It should be noted that the potentials are identical between the amorphousSiO and the equilibrium at the end of the plateau. This behavior indicates that the potential difference observed by the overpotential for the Li insertion is negligibly small, thus suggesting the high Li conduction of lithium silicate phases. Later, the potential gradually shifts to the negative range of 0.05–0.35 V. These potentials

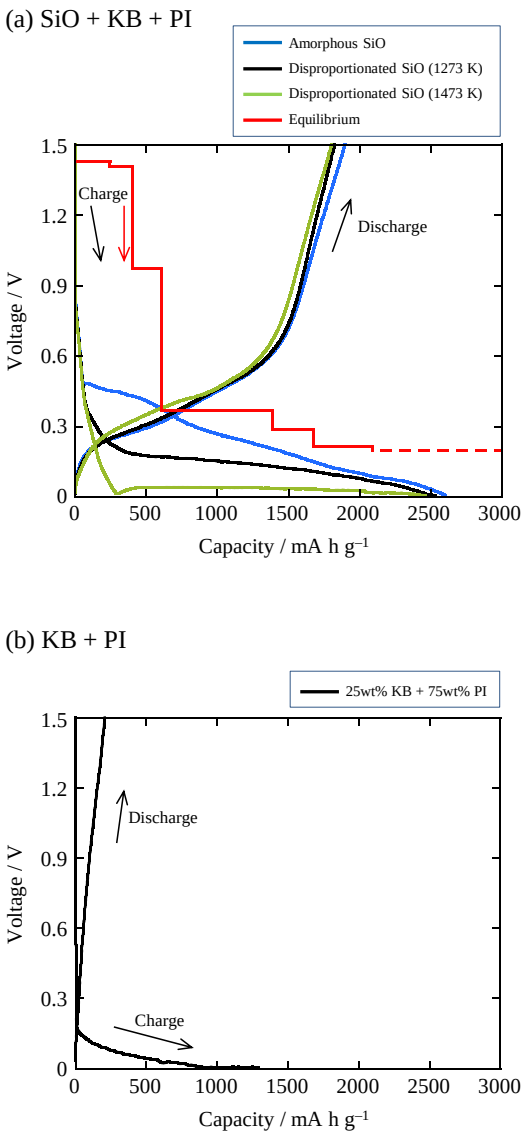

Fig. 5 (a) Charge and discharge curves for the 1st cycle of SiO/EC:DEC(1:1) + 1 mol L^{-1} $LiPF_6$/Li cells in the voltage range of 0–1.5 V at 298 K. Charge conditions: a constant current of 15 mA g^{-1} until a voltage of 0 V. Discharge conditions: a constant current of 15 mA g^{-1} until a voltage of 1.5 V. (b) Charge and discharge curves for the 1st cycle of KB+PI/EC:DEC(1:1) + 1 mol L^{-1} $LiPF_6$/Li cells in the voltage range of 0–1.5 V at 298 K. Charge conditions: a constant current of 10 mA g^{-1} until a voltage of 0 V. Discharge conditions: a constant current of 10 mA g^{-1} until a voltage of 1.5 V.

correspond to the formation of Li–Si alloys including the capacity of KB and PI. Also, the capacity should partially contain an irreversible one owing to the SEI formation at negative potentials. Even considering the charge capacity of KB conductive additive and

PI binder of 1292 mA h g^{-1} (Fig. 5(b)), which corresponds to 323 mA h $(g \cdot SiO)^{-1}$, the capacity of 2610 mA h g^{-1} is larger than the theoretical value at the start of the decomposition of Li_4SiO_4 (2090 mA h g^{-1}), suggesting the partial decomposition of lithium silicates to Li_2O. The relatively rapid potential shift after 2090 mA h g^{-1} might result from the large overpotential owing to the formed Li_2O. In contrast, the plateau that corresponds to the formation of lithium silicate is not observed for the disproportionated SiO. Especially, the charge curve for the disproportionated SiO at 1473 K shows an immediate shift to 0.02 V before 350 mA h g^{-1}. Then, the potential remains around 0.05 V, and the charge reaction finishes at 2463 mA h g^{-1}. This capacity suggests the partial decomposition of lithium silicates in addition to the formation of Li–Si alloys.

To summarize these charge behaviors, the following two points for the equilibrium and kinetics are found out. First, the equilibrium potential curve calculated from the thermodynamic data in this study is valid to discuss the reaction. Second, the overpotential for the Li insertion for lithium silicate formation, which is observed as the deviation from the equilibrium potential, is larger for the disproportionated SiO negative electrode.

4-2. Cell performance

The electrochemical behaviors of the SiO electrodes were compared at a high charge rate. The charge and discharge capacities and coulombic efficiency are summarized in Table 6. Based on the capacities shown in Tables 4 and 5, the charge reaction is expected to proceed between states ⓭ and ⓯.

Figure 6(a) shows the equilibrium potential shift until the end of the Li–Si alloy formation, with the charge curves in the initial cycle being recorded in the CC-CV mode. Here, the graphs are standardized by the capacity in each charge run. Furthermore, only

the disproportionated SiO at 1473 K shows the curve in the 2nd cycle. At a high reaction rate, the potential plateau for the formation of lithium silicate above 0.6 V is not observed. However, the charge curve shows more positive potentials for the amorphous SiO than

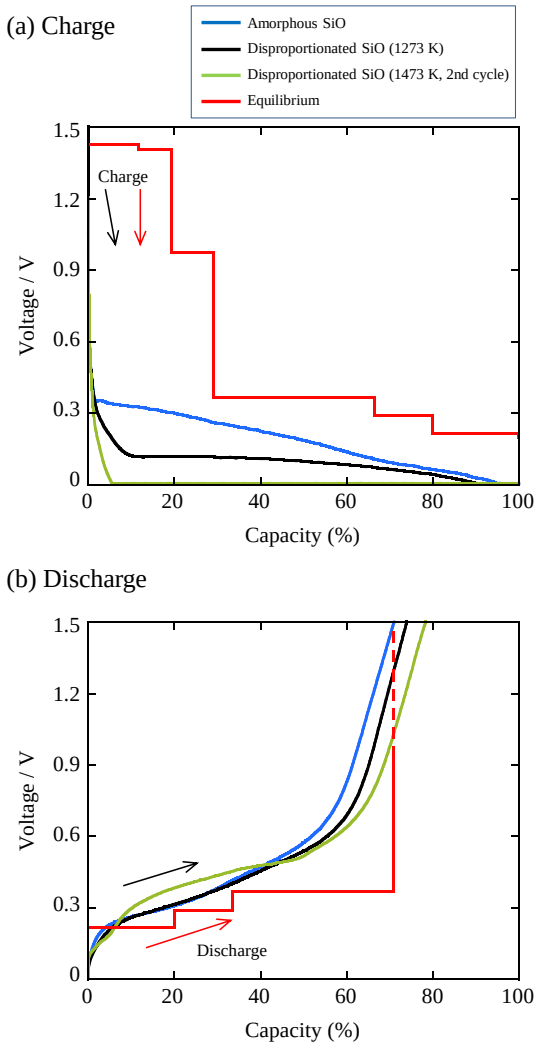

Fig. 6 (a) Charge and (b) discharge curves for the 1st cycle of SiO/EC:DEC(1:1) + 1 mol L^{-1} $LiPF_6$/Li cells in the voltage range of 0.005–1.5 V at 298 K. Charge conditions: a constant current of 150 mA g^{-1} until a voltage of 0.005 V and a constant voltage of 0.005 V until a current of 15 mA g^{-1}. Discharge conditions: a constant current of 150 mA g^{-1} until a voltage of 1.5 V.

for the disproportionated SiO electrodes. The disproportionated SiO shows such a large overpotential in the Li insertion that the 1st cycle charge reaction ends at a small capacity of 337 mA h g^{-1}, as shown in Table 6. The cause of the different overpotential is the formed phases in the 1st cycle. Only the $Li_2Si_2O_5$/Si phases are formed in the initial reaction for the amorphous SiO electrode (Fig. 7(a)). On the other hand, the reaction state starts from the mixture of Si and SiO_2 for the disproportionated SiO, and the $Li_2Si_2O_5$/Si/SiO_2 phases are formed, as shown in Fig. 7(b). The high resistivity of SiO_2 would result in the large overpotential.

In the discharge reaction for all SiO electrodes, a high discharge capacity above 1898 mA h g^{-1} and a coulombic efficiency of 71.0% were obtained. The values higher than 1482 mA h g^{-1} and 70.9% suggest that the deterioration of a SiO electrode does not occur upon decomposition of a small amount of Li_4SiO_4 in the initial cycle. The curves for the electrodes exhibit almost the same behavior with the equilibrium potentials as shown in Fig. 6(b). In spite of the slightly larger discharge capacity, the curve for the disproportionated SiO at 1473 K shows a more positive potential than the other electrodes and the equilibrium curve. This behavior is also explained by the high resistivity and large overpotential of the electrodes.

Table 6 Charge and discharge capacities and coulombic efficiency for the 1st cycle of SiO/EC:DEC(1:1) + 1 mol L^{-1} $LiPF_6$/Li cells in the voltage range of 0.005–1.5 V at 298 K.

	Charge Capacity, C_c mAh g^{-1}	Discharge Capacity, C_d mAh g^{-1}	Coulombic efficiency (%)
Amorphous SiO	2753	1955	71.0
1273 K heat treatment	2623	1898	72.4
1473 K heat treatment	337 (2554)	132 (2001)	39.1 (78.4)

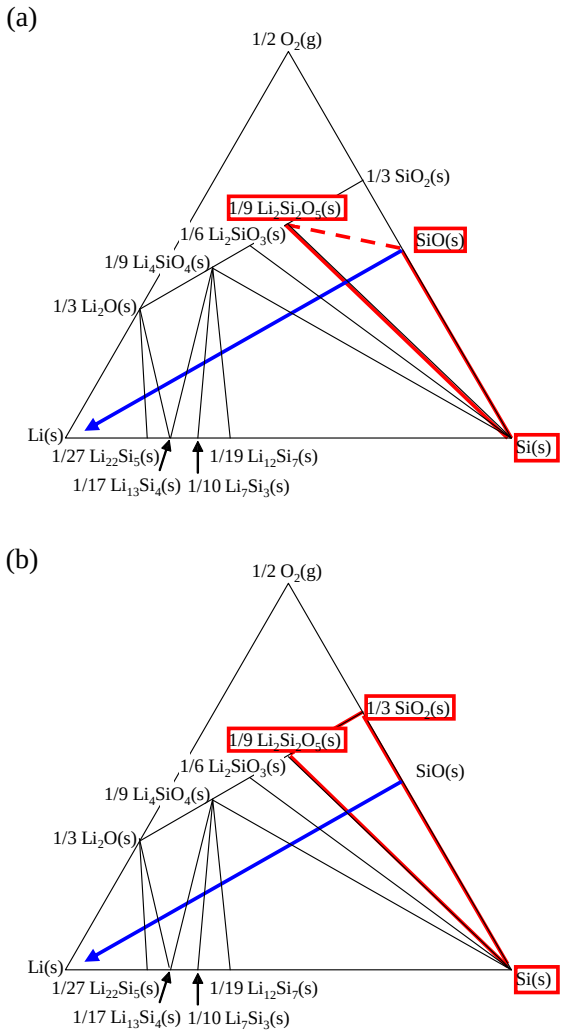

Fig. 7 Comparison of transition of formed phases during the Li insertion for (a) amorphous and (b) disproportionated SiO negative electrodes at 298 K.

The charge/discharge curves for the 2nd and 10th cycles are compared in Figs. 8(a) and (b), respectively. Also in these graphs, the curves for the 3rd and 11th cycle are shown for the disproportionated SiO at 1473 K. Compared to the behaviors in the 1st cycle in Fig. 6, all the SiO electrodes indicate almost the same potential curves in the charge reaction, which are similar with the 1st cycle behavior for the amorphous SiO. As a result of lithium silicate formation during the 1st cycle, the overpotential for Li

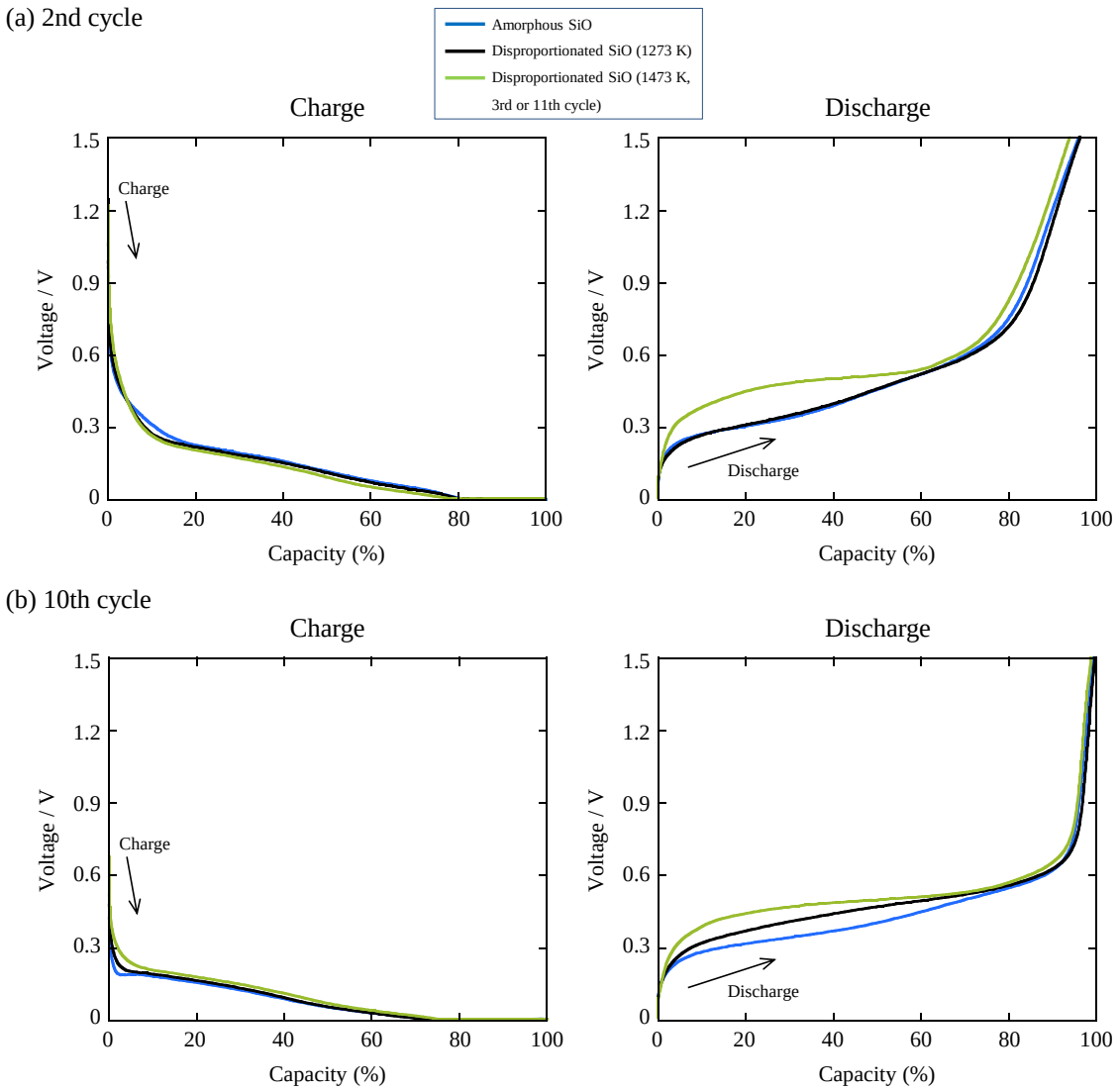

Fig. 8 Charge and discharge curves for the (a) 2nd and (b) 10th cycles of SiO/EC:DEC(1:1) + 1 mol L^{-1} $LiPF_6$/Li cells in the voltage range of 0.005–1.5 V at 298 K. Charge conditions (2nd cycle): a constant current of 450 mA g^{-1} until a voltage of 0.005 V and a constant voltage of 0.005 V until a current of 15 mA g^{-1}. Charge conditions (after 3rd cycle): a constant current of 750 mA g^{-1} until a voltage of 0.005 V and a constant voltage of 0.005 V until a current of 15 mA g^{-1}. Discharge conditions (2nd cycle): a constant current of 450 mA g^{-1} until a voltage of 1.5 V. Discharge conditions (after 3rd cycle): a constant current of 750 mA g^{-1} until a voltage of 1.5 V.

insertion became small even for the disproportionated SiO. However, the overpotential for the discharge reaction remains larger for the disproportionated SiO electrodes. With the repetition of cycles, the disproportionated SiO experiences a potential shift to the

positive direction – i.e., a smaller power density. One possible explanation for this behavior concerns the slow kinetics for the discharge reaction; that is because the inhomogeneous formation of $Li_2Si_2O_5$/Si/SiO_2 phases disturbs a Li extraction owing to the SiO_2 phase. The homogeneous formation of Li–Si alloys and lithium silicates in a nano scale for the amorphous SiO electrode would enable a faster Li diffusion in the discharge reaction compared to the disproportionated SiO producing large-sized SiO_2 and Li_2O.

Conclusion

The electrochemical behavior of a SiO negative electrode was investigated based on the calculated equilibrium curves. The ternary phase diagram for the Li–Si–O system at 298 K was calculated, and the equilibrium potentials for Li insertion/extraction reactions were diagrammatically indicated. The formation of lithium silicates is the initial reaction of the SiO electrodes, and occurs above 0.36 V vs. Li/Li^+; furthermore, the decomposition of lithium silicates starts after the formation of the $Li_{13}Si_4$ alloy. The kinetics was discussed from the experimental curves of the SiO electrodes with reference to the equilibria. It was suggested that the Li_4SiO_4 phase formed as an irreversible component had high Li conduction . The disproportionated SiO electrode demonstrated a larger overvoltage than the amorphous SiO owing to the formation of SiO_2. While the overvoltage became identical in the charge reaction between the amorphous and disproportionated SiO electrodes, a large overpotential (thus resulting in a smaller power density) was observed for the disproportionated SiO in the discharge reaction.

Acknowledgments

The authors would like to thank Assistant Professor Naoyuki Hatada at Kyoto University for the use of Chesta ver. 2.22, and Editage (www.editage.jp) for English language editing.

References

1 J. Cabana, L. Monconduit, D. Larcher, M. R. Palacín, Adv. Mater. 22 (2010) E170–E192.

2 C.-M. Park, J.-H. Kim, H. Kim, H.-J. Sohn, Chem. Soc. Rev. 39 (2010) 3115–3141.

3 M. V. Reddy, G. V. Subba Rao, B. V. R. Chowdari, Chem. Rev. 113 (2013) 5364–5457.

4 T. B. Massalski, H. Okamoto, P. R. Subramanian, L. Kacprzak, eds., Binary Alloy Phase Diagrams, 2nd ed., ASM International, Metals Park, Ohio, 1990.

5 R. J. Temkin, J. Non-Cryst. Solids 17 (1975) 215–230.

6 A. Hohl, T. Wieder, P. A. van Aken, T. E. Weirich, G. Denninger, M. Vidal, S. Oswald, C. Deneke, J. Mayer, H. Fuess, J. Non-Cryst. Solids 320 (2003) 255–280.

7 H. R. Philipp, J. Non-Cryst. Solids 8–10 (1972) 627–632.

8 H. R. Philipp, J. Phys. Chem. Solids 32 (1971) 1935–1945.

9 K. Schulmeister, W. Mader, J. Non-Cryst. Solids 320 (2003) 143–150.

10 J. Wang, X. F. Wang, Q. Li, A. Hryciw, A. Meldrum, Philos. Mag. 87 (2007) 11–27.

11 B. Hallstedt, Calphad 16 (1992) 53–61.

12 F. T. Ferguson, J. A. Nuth, III, J. Chem. Eng. Data 57 (2012) 721–728.

13 S. M. Schnurre, J. Gröbner, R. Schmid-Fetzer, J. Non-Cryst. Solids 336 (2004) 1–25.

14 M. Mamiya, H. Takei, M. Kikuchi, C. Uyeda, J. Cryst. Growth 229 (2001) 457–461.

15 M. Mamiya, M. Kikuchi, H. Takei, J. Cryst. Growth 237–239 (2002) 1909–1914.

16 A. Barranco, F. Yubero, J. P. Espinos, J. P. Holgado, A. Caballero, A. R. Gonzalez-Elipe, J. A. Mejias, Vacuum 67 (2002) 491–499.

17 R. Alfonsetti, L. Lozzi, M. Passacantando, P. Picozzi, S. Santucci, Appl. Surf. Sci. 70–71 (1993) 222–225.

18 A. Hirata, S. Kohara, T. Asada, M. Arao, C. Yogi, H. Imai, Y. Tan, T. Fujita, M. Chen, Nat. Commun. 7 (2016) 11591.

19 J. Yang, Y. Takeda, N. Imanishi, C. Capiglia, J. Y. Xie, O. Yamamoto, Solid State Ionics 152–153 (2002) 125–129.

20 Y. Nagao, H. Sakaguchi, H. Honda, T. Fukunaga, T. Esaka, J. Electrochem. Soc., 151 (2004) A1572–A1575.

21 M. Miyachi, H. Yamamoto, H. Kawai, T. Ohta, M. Shirakata, J. Electrochem. Soc. 152 (2005) A2089–A2091.

22 M. Miyachi, H. Yamamoto, H. Kawai, J. Electrochem. Soc. 154 (2007) A376–A380.

23 T. Kim, S. Park, S. M. Oh, J. Electrochem. Soc. 154 (2007) A1112–A1117.

24 Y. Yamada, Y. Iriyama, T. Abe, Z. Ogumi, J. Electrochem. Soc. 157 (2010) A26–A30.

25 C.-M. Park, W. Choi, Y. Hwa, J.-H. Kim, G. Jeong, H.-J. Sohn, J. Mater. Chem. 20 (2010) 4854–4860.

26 S. Komaba, K. Shimomura, N. Yabuuchi, T. Ozeki, H. Yui, K. Konno, J. Phys. Chem. C 115 (2011) 13487–13495.

27 J.-H. Kim, C.-M. Park, H. Kim, Y.-J. Kim, H.-J. Sohn, J. Electroanal. Chem. 661 (2011) 245–249.

28 H. Yamamura, K. Nobuhara, S. Nakanishi, H. Iba, S. Okada, J. Ceram. Soc. Jpn. 119 (2011) 855–860.

29 T. Miyuki, Y. Okuyama, T. Sakamoto, Y. Eda, T. Kojima, T. Sakai, Electrochemistry 80 (2012) 401–404.

30 G. Jeong, J.-H. Kim, Y.-U. Kim, Y.-J. Kim, J. Mater. Chem. 22 (2012) 7999–8004.

31 K. W. Kim, H. Park, J. G. Lee, J. Kim, Y.-U. Kim, J. H. Ryu, J. J. Kim, S. M. Oh, Electrochim. Acta 103 (2013) 226–230.

32 H. Takezawa, K. Iwamoto, S. Ito, H. Yoshizawa, J. Power Sources 244 (2013) 149–157.

33 T. Morita, N. Takami, J. Electrochem. Soc. 153 (2006) A425–A430.

34 J.-H. Kim, H.-J. Sohn, H. Kim, G. Jeong, W. Choi, J. Power Sources 170 (2007) 456–459.

35 Y. Kobayashi, S. Seki, Y. Mita, Y. Ohno, H. Miyashiro, P. Charest, A. Guerfi, K. Zaghib, J. Power Sources 185 (2008) 542–548.

36 A. Velucharmy, C.-H. Doh, D.-H. Kim, J.-H. Lee, D.-J. Lee, K.-H. Ha, H.-M. Shin, B.-S. Jin, H.-S. Kim, S.-I. Moon, C.-W. Park, J. Power Sources 188 (2009) 574–577.

37 M. Yamada, A. Ueda, K. Matsumoto, T. Ohzuki, J. Electrochem. Soc. 158 (2011) A417–A421.

38 J. Wang, H. Zhao, J. He, C. Wang, J. Wang, J. Power Sources 196 (2011) 4811–4815.

39 A. Guerfi, P. Charest, M. Dontigny, J. Trottier, M. Lagacé, P. Hovington, A. Vijh, K. Zaghib, J. Power Sources 196 (2011) 5667–5673.

40 Q. Si, K. Hanai, T. Ichikawa, M. B. Phillipps, A. Hirano, N. Imanishi, O. Yamamoto, Y. Takeda, J. Power Sources 196 (2011) 9774–9779.

41 Y. Ren, J. Ding, N. Yuan, S. Jia, M. Qu, Z. Yu, J. Solid State Electrochem. 16 (2012) 1453–1460.

42 C. Guo, D. Wang, Q. Wang, B. Wang, T. Liu, Int. J. Electrochem. Sci. 7 (2012) 8745–8752 .

43 H. Sepehri-Amin, T. Ohkubo, M. Kodzuka, H. Yamamura, T. Saito, H. Iba, K. Hono, Scripta Materialia 69 (2013) 92–95.

44 Q. Yuan, F. Zhao, Y. Zhao, Z. Liang, D. Yan, Electrochim. Acta 115 (2014) 16–21.

45 Y. Yang, W. Peng, H. Guo, Z. Wang, X. Li, Y. Zhou, Y. Liu, Trans. Nonferrous Met. Soc. China 17 (2007) 1339–1342.

46 B. Guo, J. Shu, Z. Wang, H. Yang, L. Shi, Y. Liu, L. Chen, Electrochem. Commun. 10 (2008) 1876–1878.

47 Q. Sun, B. Zhang, Z.-W. Fu, Appl. Sur. Sci. 254 (2008) 3774–3779.

48 Y. Yao, J. Zhang, L. Xue, T. Huang, A. Yu, J. Power Sources 196 (2011) 10240–10243.

49 C. Ban, B. B. Kappes, Q. Xu, C. Engtrakul, C. V. Ciobanu, A. C. Dillon, Y. Zhao, Appl. Phys. Lett. 100 (2012) 243905.

50 Y. Zhang, Y. Li, Z. Wang, K. Zhao, Nano Lett. 14 (2014) 7161–7170.

51 M. Yamada, A. Inaba, S. Nagayama, K. Matsumoto, A. Ueda, T. Ohzuku, Meeting Abstract of The 50th Battery Symposium in Japan, Nov. 30–Dec. 2, Kyoto, Japan, 2009, p. 191.

52 Y. Hwa, C.-M. Park, H.-J. Sohn, J. Power Sources 222 (2013) 129–134.

53 X. Yang, Z. Wen, L. Zhang, M. You, J. Alloy Compd. 464 (2008) 265–269.

54 H. Migge, J. Nucl. Mater. 151 (1988) 101–107.

55 O. Götzmann, J. Nucl. Mater. 167 (1989) 213–224.

56 J. Sangster, A.D. Pelton, J. Phase Equilibria 13 (1992) 296–299.

57 H. A. Wrledt, Bulletin of Alloy Phase Diagrams 11 (1990) 43–61.

58 H. Okamoto, J. Phase Equilibria Diffusion 28 (2007) 309–310.

59 R. S. Roth, ed., Phase Equilibria Diagrams: Phase Diagrams for Ceramists, American Ceramic Society, Waterville, Ohio, 1995.

60 S. S. Kim, T. H. Sanders, Jr., J. Am. Ceram. Soc. 74 (1991) 1833–1840.

61 A. Skokan, H. Wedemeyer, D. Vollath, E. Günther, Proc. 14th Symp. on Fusion Technology, Avignon, p. 1255 (1986).

62 H. Okamoto, Bull. Alloy Phase Diagrams 11 (1990) 306–312.

63 HSC Chemistry® ver. 5.1, Outokumpu Research Oy, Poly, Finland, 2002.

64 I. Barin, Thermochemical Data of Pure Substances, VCH Verlags Gesellschaft, Weinheim, 1993.

65 A. J. Bard, R. Parsons, J. Jordan, Standard potentials in aqueous solution, Marcel Dekker Inc., New York, 1985.

66 Landolt-Börnstein: Thermodynamic Properties of Inorganic Material, Scientific Group Thermodata Europe (SGTE), Springer-Verlag, Berlin-Heidelberg, Part 1, 1999.

67 O. Knacke, O. Kubaschewski, K. Hesselman: Thermochemical Properties of Inorganic Substances, 2nd ed., Springer-Verlag, Berlin, 1991.

68 B. J. Mcbride, S. Gordon, M. A. Reno, eds., Thermodynamic Data for Fifty Reference Elements, NASA-TP-3287, N93-19977, 1993.

69 Glushko Thermocenter of the Russian Academy of Sciences, IVTAN Association, Izhorskaya 13/19, 127412 Moscow, Russia, 1994.

70 Landolt-Börnstein: Thermodynamic Properties of Inorganic Material, Scientific Group Thermodata Europe (SGTE), Springer-Verlag, Berlin-Heidelberg, Part 4, 2001.

71 I. Barin, Thermochemical Data of Pure Substances, VCH Verlags Gesellschaft, Weinheim, 1989.

72 I. Barin, O. Knacke, O. Kubaschewski: Thermochemical Properties of Inorganic Substances, Supplement, Springer-Verlag, Berlin, 1977, p. 861.

73 S. C. Lai, J. Electrochem. Soc. 123 (1976) 1196–1197.

74 R. A. Sharma, R. N. Seefurth, J. Electrochem. Soc. 123 (1976) 1763–1768.

75 V. P. Nikolaiev, A. G. Morachevskii, A. I. Demidov, E. V. Bairachnyi, Zh. Prikl. Khim. 53 (1980) 2088–2090.

76 C. J. Wen, R. A. Huggins, J. Solid State Chem. 37 (1981) 271–278.

77 K. Amezawa, N. Yamamoto, Y. Tomii, Y. Ito, J. Electrochem. Soc. 145 (1998) 1986–1993.

78 A. I. Demidov, A. G. Morachevskii, V. P. Nikolaev, N. V. Berenda, Russ. J. Appl. Chem. 61 (1988) 1373–1375.

79 M. H. Braga, L. F. Malheiros, I. Ansara, J. Phase Equilib. 16 (1995) 324–330.

80 N. Hatada, Chesta ver. 2.22, Department of Materials Science and Engineering, Kyoto University, Japan. http://www.aqua.mtl.kyoto-u.ac.jp/chestaEng.html.

81 S. C. Jung, H.-J. Kim, J.-H. Kim, Y.-K. Han, J. Phys. Chem. C 120 (2016) 886–892.

Table(s)

Table 1 Representative reports on battery and electrode characteristics of the SiO negative electrode.

Author, Ref.	Year	SiO phase	Intermediate phase	Initial charge capacity (mAh g^{-1})	Initial discharge capacity (mAh g^{-1})	Initial coulombic efficiency (%)	Note
Yang et al. [19]	2002	Amor.	-	ca. 2250	ca. 1300	ca. 57.8	-
Nagao et al. [20]	2004	Amor.	SiO_2	1594	-	-	Neutron elastic scattering
Miyachi et al. [21]	2005	Amor.	Li–Si–O, Li_2O	2404	598	24.9	XPS
Miyachi et al. [22]	2007	-	Li–Si–O, Li_2O	2520	1260	50.0	Metal-doped SiO, XPS
Kim et al. [23]	2007	-	Li–Si–O, Li_2O	2680	1470	54.9	NMR, HR-TEM, electrochemical dilatometry. Plateau at 0.8 V vs. Li^+/Li in 1st discharge
Yamada et al. [24]	2007	-	-	-	-	-	Kinetics evaluation by AC impedance spectroscopy
Park et al [25]	2010	Amor./ dispro.	SiO_x	2216/ 185	1104/ 94	49.8/ 50.8	TEM, Disproportionated at 800, 1000, and 1200 ºC.
Komaba et al [26]	2011	-	-	ca. 1800	826	45.9	-
Kim et al., [27]	2011	Amor./ dispro.	Li–Si–O, Li_2O	2410	1300	53.9	NMR, HR-TEM, Differential capacity peaks at 0.08 and 0.24 V vs. Li^+/Li
Yamamura et al. [28]	2011	Dispro.	Li–Si–O	2548	1791	70.3	Plateau at 0.2 and 0.5 V vs. Li^+/Li in 1st discharge. First principles calculation. SiO_2 was also reacted.
Miyuki et al. [29]	2011	Amor./ dispro.	-	-	-	-	$LiFePO_4$/SiO full cell.
Jeong et al. [30]	2012	Dispro.	-	1757	1265	72.0	TiO_2 coated SiO
Kim et al. [31]	2013	Dispro.	-	1958	1413	72.2	Carbon coated SiO. Differential capacity peaks at 0.06, 0.21, 0.31 and 0.48 V vs. Li^+/Li after 5th cycle
Takezawa et al. [32]	2013	Amor.	Li–Si–O, Li_2O	2418	1306	54.0	SiO_x ($0.17 < x < 1.34$) was used. XPS

-: Not given

Table(s)

Table 2 Thermodynamic data for Li–Si–O system at 298 K used for the calculation.

Compound				Standard Gibbs energy, G° / kJ mol^{-1}	Standard Gibbs energy of formation, ΔG_f° / kJ mol^{-1}	Ref
Formula	Component					
	Li	Si	O			
Li	1	0	0	–8.7	0	[64–66]
Si	0	1	0	–5.6	0	[67]
O_2	0	0	2	–61.1	0	[66,68]
$Li_{12}Si_7$	12	7	0	–570.5	–426.9	Calculated from [79]
Li_7Si_3	7	3	0	–312.7	–235.0	
$Li_{13}Si_4$	13	4	0	–525.6	–390.1	
$Li_{22}Si_5$	22	5	0	–758.8	–539.4	
Li_2O	2	0	1	–609.1	–561.2	[64,69 ,70]
SiO_2	0	1	2	–923.2	–856.5	[71]
$Li_2Si_2O_5$	2	2	5	–2598.3	–2416.9	[64]
Li_2SiO_3	2	1	3	–1673.4	–1558.8	[67]
Li_4SiO_4	4	1	4	–2366.2	–2203.6	[72]

Table(s)

Table 3 Equilibrium phases and electrode potentials during the Li insertion for a SiO negative electrode at 298 K.

	Equilibrium phases			Activity or pressure				Equilibrium potential, E, / V (vs. Li^+/Li)
				log p_{O2}	log a_{Si}	log a_{Li}	a_{Li}	
①	Si	SiO_2						
②	Si	SiO_2	$Li_2Si_2O_5$	–150.1	0	–24.2	6.9×10^{-25}	1.428
③	Si	$Li_2Si_2O_5$						↓
④	Si	$Li_2Si_2O_5$	Li_2SiO_3	–150.4	0	–23.8	1.6×10^{-24}	1.406
⑤	Si	Li_2SiO_3						↓
⑥	Si	Li_2SiO_3	Li_4SiO_4	–160.2	0	–16.5	3.4×10^{-17}	0.973
⑦	Si	Li_4SiO_4						↓
⑧	Si	$Li_{12}Si_7$	Li_4SiO_4	–180.6	0	–6.24	5.8×10^{-17}	0.368
⑨	$Li_{12}Si_7$	Li_4SiO_4						↓
⑩	$Li_{12}Si_7$	Li_7Si_3	Li_4SiO_4	–182.1	–2.27	–4.91	1.2×10^{-5}	0.290
⑪	Li_7Si_3	Li_4SiO_4						↓
⑫	Li_7Si_3	$Li_{13}Si_4$	Li_4SiO_4	–183.2	–5.17	–3.67	2.1×10^{-4}	0.217
⑬	$Li_{13}Si_4$	Li_4SiO_4						↓
⑭	$Li_{13}Si_4$	Li_4SiO_4	Li_2O	–183.3	–6.21	–3.35	4.5×10^{-4}	0.198
⑮	$Li_{13}Si_4$	Li_2O						↓
⑯	$Li_{13}Si_4$	$Li_{22}Si_5$	Li_2O	–190.4	–12.0	–1.58	2.7×10^{-2}	0.093
⑰	$Li_{22}Si_5$	Li_2O						↓
⑱	$Li_{22}Si_5$	Li_2O	Li	–196.7	–18.9	0	1	0

Table(s)

Table 4 The calculated reactions for the Li insertion of a SiO negative electrode at 298 K.

	Reaction	Atomic ratio of Li with respect to SiO	Charge capacity, C_c / mA h g^{-1}
③	$5SiO + 2Li^+ + 2e^- \rightarrow 3Si + Li_2Si_2O_5$	0.40	243
⑤	$3SiO + 2Li^+ + 2e^- \rightarrow 2Si + Li_2SiO_3$	0.67	405
⑦	$4SiO + 4Li^+ + 4e^- \rightarrow 3Si + Li_4SiO_4$	1.00	608
⑨	$28SiO + 64Li^+ + 64e^- \rightarrow 3Li_{12}Si_7 + 7Li_4SiO_4$	2.29	1390
⑪	$12SiO + 33Li^+ + 33e^- \rightarrow 3Li_7Si_3 + 3Li_4SiO_4$	2.75	1672
⑬	$16SiO + 55Li^+ + 55e^- \rightarrow 3Li_{13}Si_4 + 4Li_4SiO_4$	3.44	2090
⑮	$4SiO + 21Li^+ + 21e^- \rightarrow Li_{13}Si_4 + 4Li_2O$	5.25	3192
⑰	$5SiO + 32Li^+ + 32e^- \rightarrow Li_{22}Si_5 + 5Li_2O$	6.40	3891

Table(s)

Table 5 The calculated reactions for the Li extraction of a SiO negative electrode at 298 K.

Charged state	Dis-charged state	Reaction	Atomic ratio of Li with respect to SiO	Discharge capacity, C_d / mA h g^{-1}	Coulombic efficiency (%)
⑬	⑪	$3Li_{13}Si_4 + 4Li_4SiO_4 \rightarrow 4Li_7Si_3 + 4Li_4SiO_4 + 11Li^+ + 11e^-$	0.69	418	20.0
	⑨	$21Li_{13}Si_4 + 28Li_4SiO_4 \rightarrow 12Li_{12}Si_7 + 28Li_4SiO_4 + 129Li^+ + 129e^-$	1.15	700	33.5
	⑦	$3Li_{13}Si_4 + 4Li_4SiO_4 \rightarrow 12Si + 4Li_4SiO_4 + 39Li^+ + 39e^-$	2.44	1482	70.9
⑮		$Li_{13}Si_4 + 4Li_2O \rightarrow 3Si + Li_4SiO_4 + 17Li^+ + 17e^-$	4.25	2584	81.0
⑰		$4Li_{22}Si_5 + 20Li_2O \rightarrow 15Si + 5Li_4SiO_4 + 108Li^+ + 108e^-$	5.40	3283	84.4

Table(s)

Table 6 Charge and discharge capacities and coulombic efficiency for the 1st cycle of SiO/EC:DEC(1:1) + 1 mol L^{-1} $LiPF_6$/Li cells in the voltage range of 0.005–1.5 V at 298 K.

	Charge Capacity, C_c mAh g^{-1}	Discharge Capacity, C_d mAh g^{-1}	Coulombic efficiency (%)
Amorphous SiO	2753	1955	71.0
1273 K heat treatment	2623	1898	72.4
1473 K heat treatment	337 (2554)	132 (2001)	39.1 (78.4)

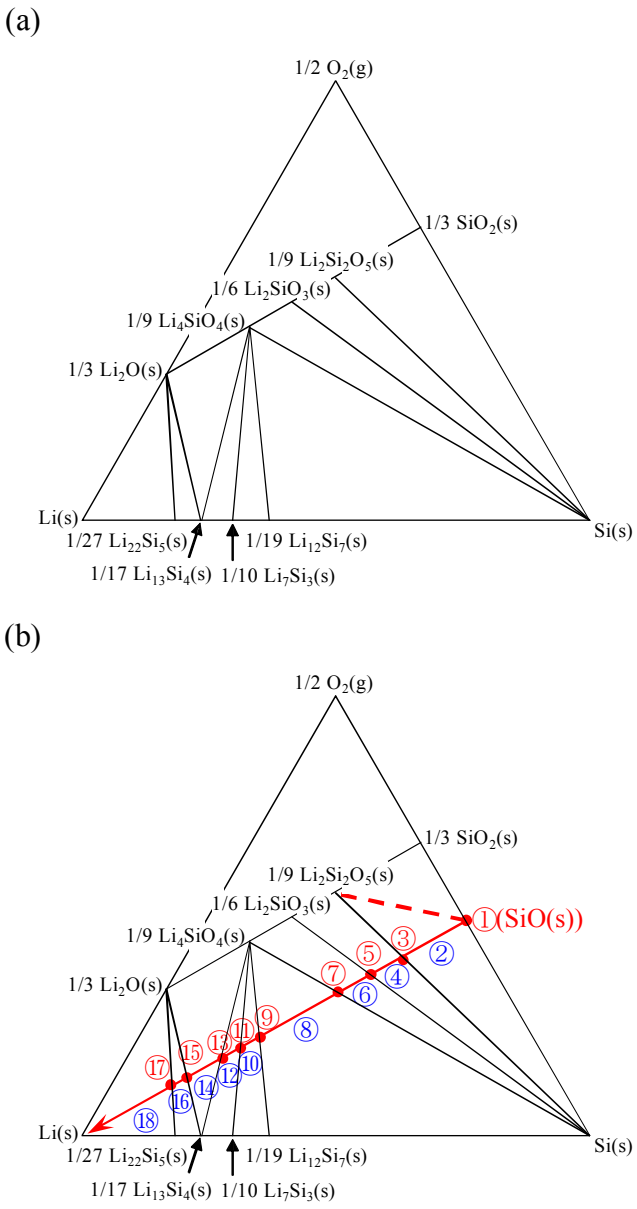

Fig. 1 (a) Calculated ternary phase diagram for the Li–Si–O system at 298 K. (b) Transition of formed phases during the Li insertion for a SiO negative electrode at 298 K shown in the ternary phase diagram for Li–Si–O system.

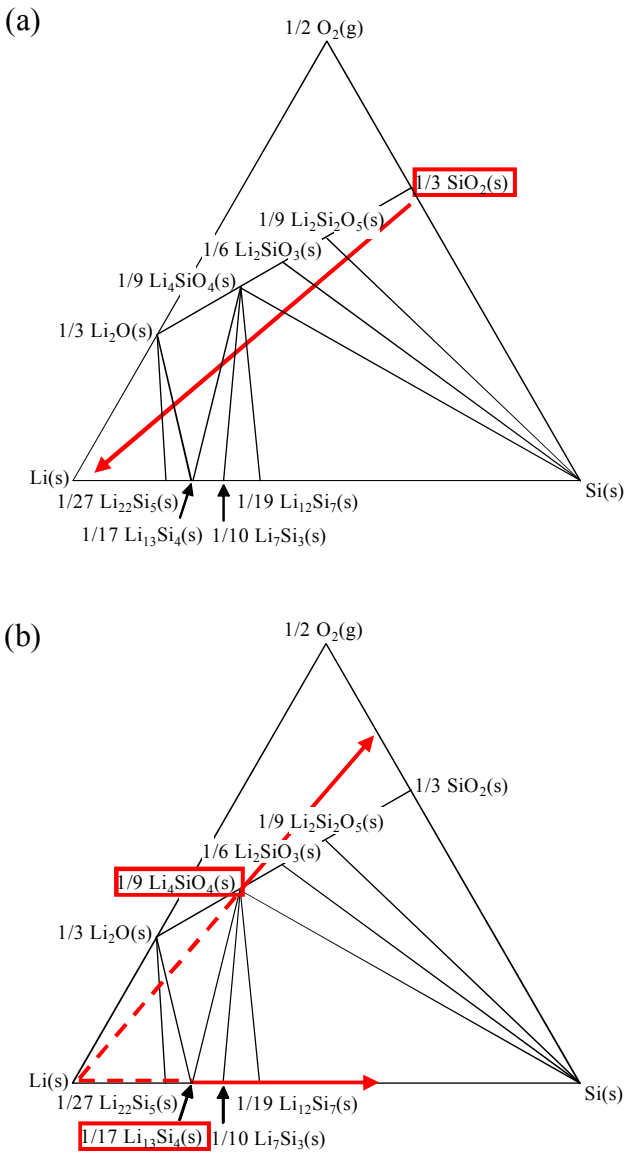

Fig. 2 Reaction pathway during (a) the Li insertion for a SiO_2 negative electrode and (b) the Li desertion for a Li_4SiO_4 electrode at 298 K shown in the ternary phase diagram for Li–Si–O system.

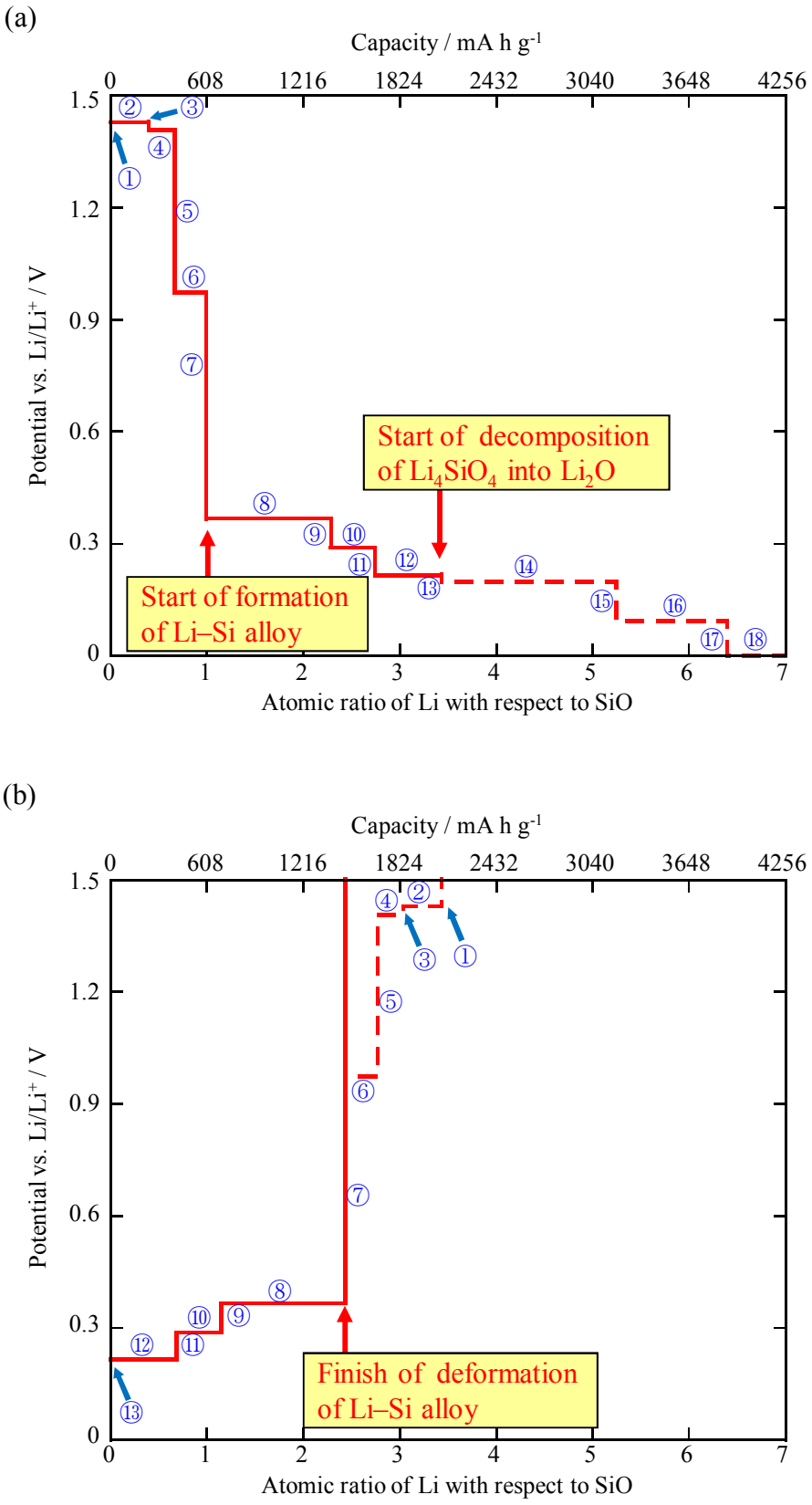

Fig. 3 Transition of equilibrium electrode potential during the Li (a) insertion and (b) desertion after the formation of $Li_{13}Si_4$ for a SiO negative electrode at 298 K shown in the ternary phase diagram for Li–Si–O system.

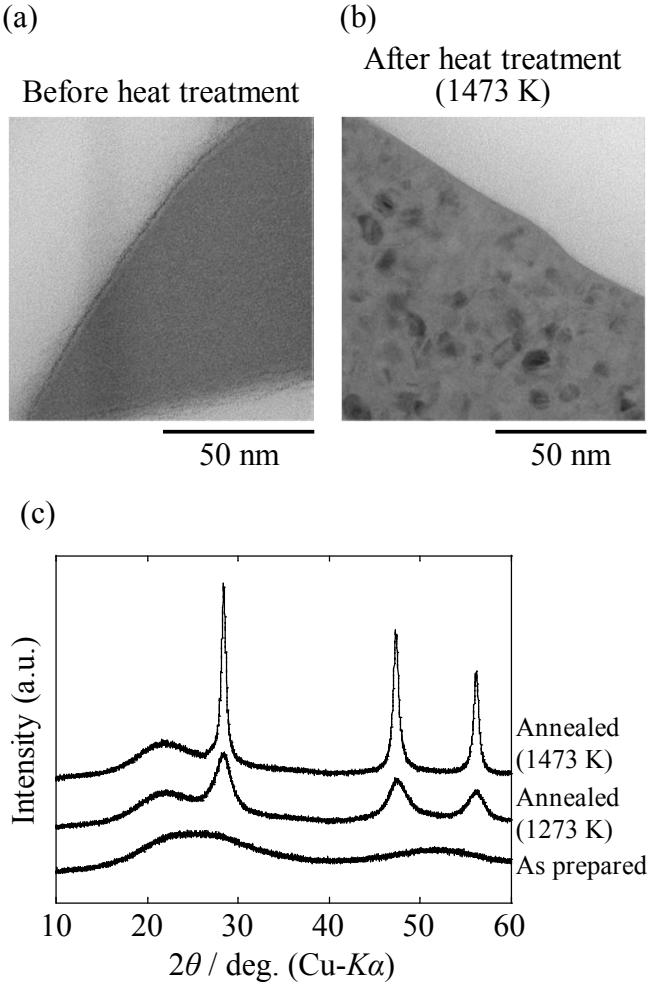

Fig. 4 (a, b) TEM images and (c) XRD patterns for the silicon monoxide particles before and after the heat treatment in an Ar atmosphere at 1273 K and 1473 K.

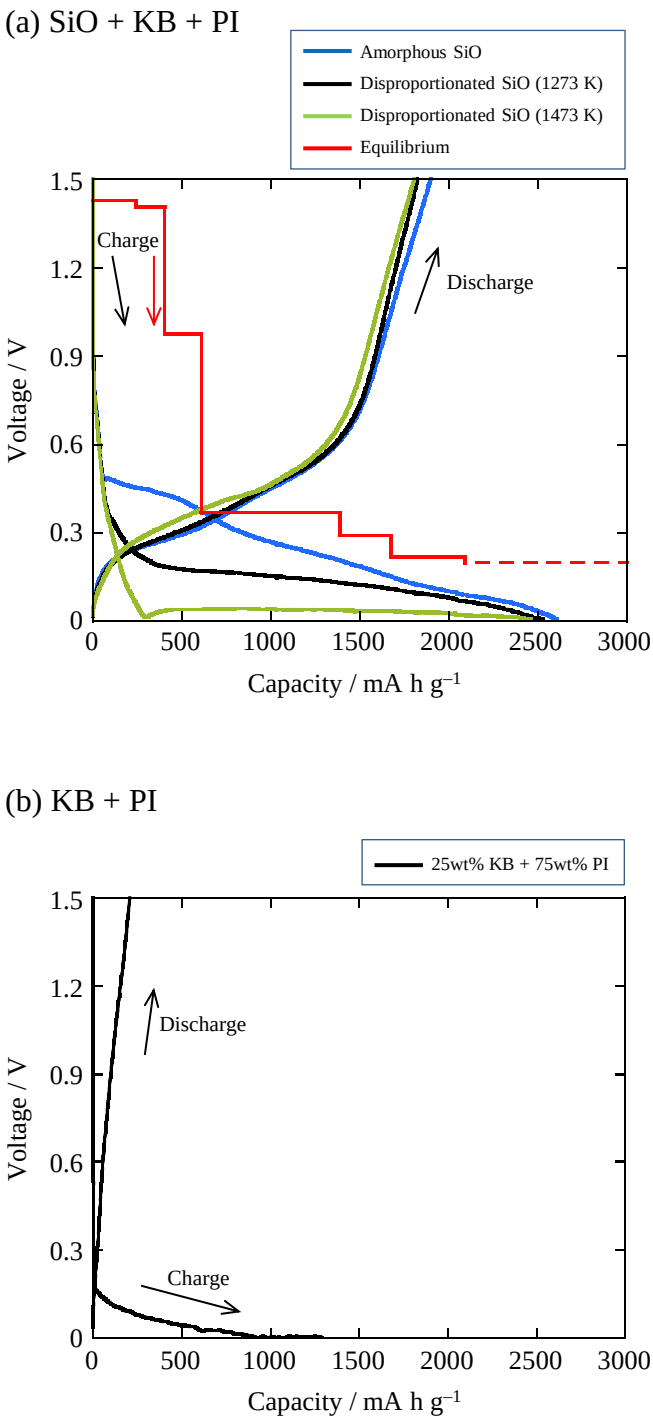

Fig. 5 (a) Charge and discharge curves for the 1st cycle of SiO/EC:DEC(1:1) + 1 mol L^{-1} $LiPF_6$/Li cells in the voltage range of 0–1.5 V at 298 K. Charge conditions: a constant current of 15 mA g^{-1} until a voltage of 0 V. Discharge conditions: a constant current of 15 mA g^{-1} until a voltage of 1.5 V. (b) Charge and discharge curves for the 1st cycle of KB+PI/EC:DEC(1:1) + 1 mol L^{-1} $LiPF_6$/Li cells in the voltage range of 0–1.5 V at 298 K. Charge conditions: a constant current of 10 mA g^{-1} until a voltage of 0 V. Discharge conditions: a constant current of 10 mA g^{-1} until a voltage of 1.5 V.

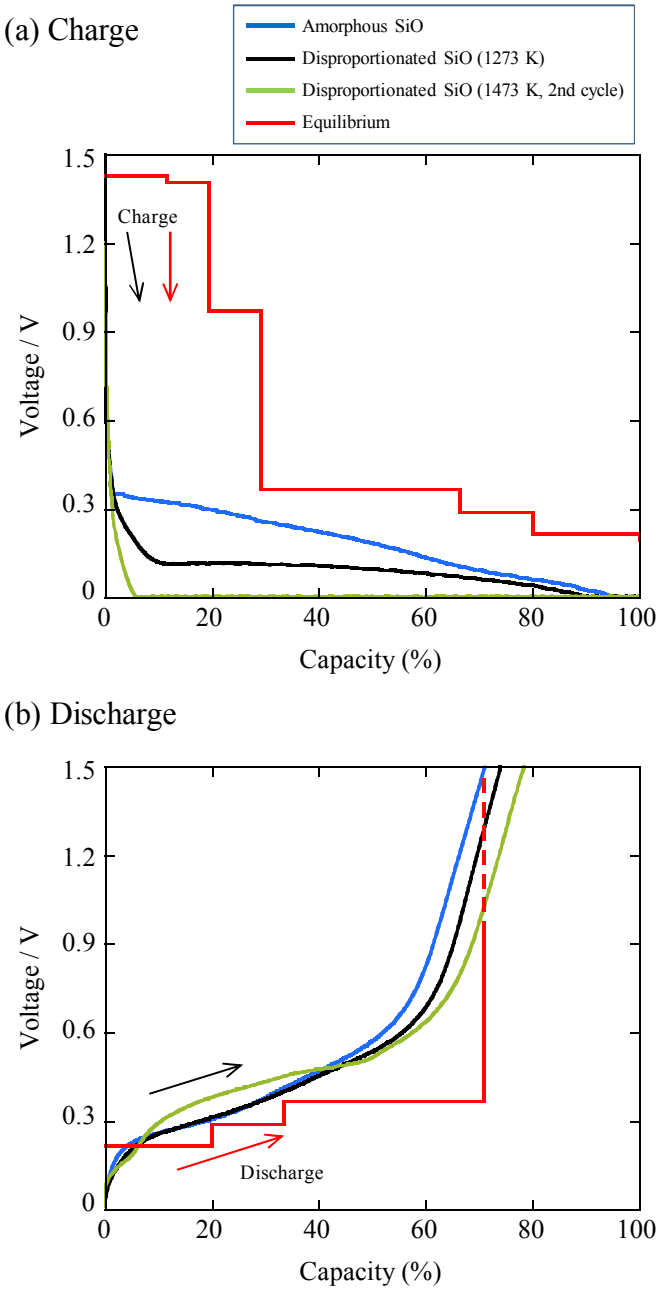

Fig. 6 (a) Charge and (b) discharge curves for the 1st cycle of SiO/EC:DEC(1:1) + 1 mol L^{-1} $LiPF_6$/Li cells in the voltage range of 0.005–1.5 V at 298 K. Charge conditions: a constant current of 150 mA g^{-1} until a voltage of 0.005 V and a constant voltage of 0.005 V until a current of 15 mA g^{-1}. Discharge conditions: a constant current of 150 mA g^{-1} until a voltage of 1.5 V.

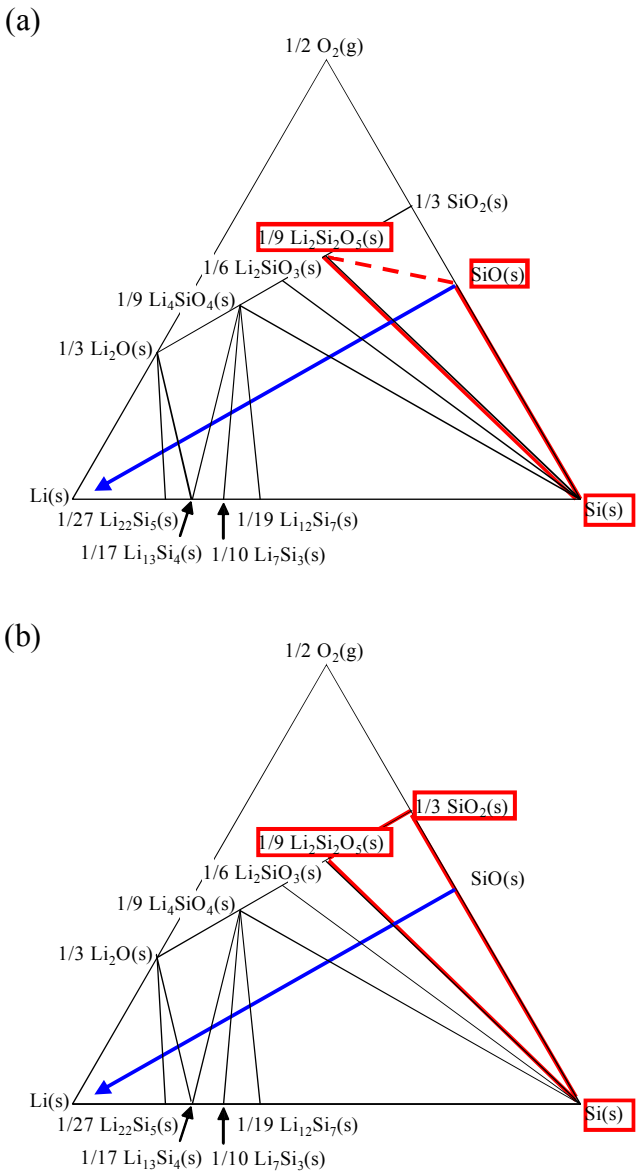

Fig. 7 Comparison of transition of formed phases during the Li insertion for (a) amorphous and (b) disproportionated SiO negative electrodes at 298 K.

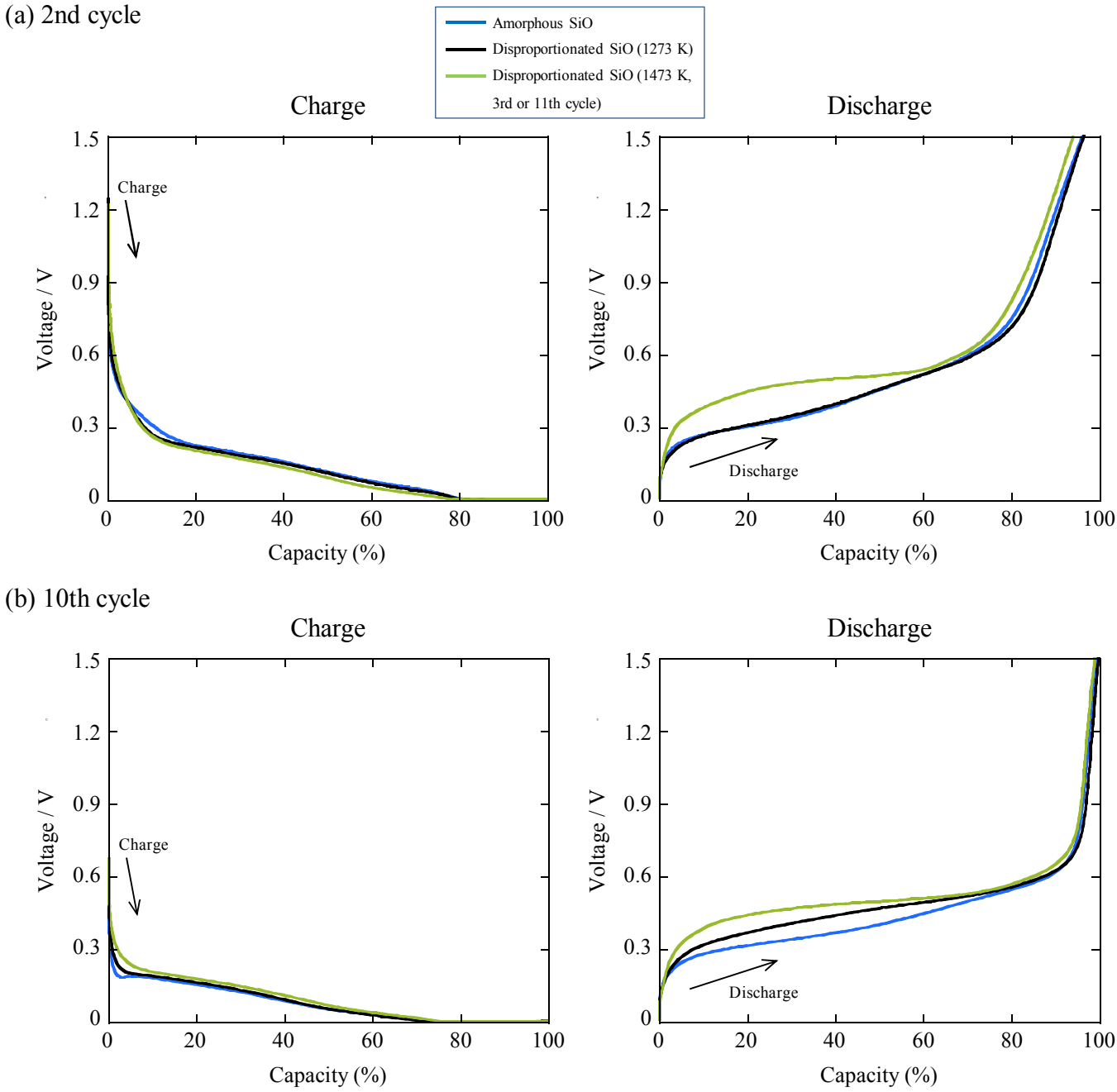

Fig. 8 Charge and discharge curves for the (a) 2nd and (b) 10th cycles of SiO/EC:DEC(1:1) + 1 mol L^{-1} $LiPF_6$/Li cells in the voltage range of 0.005–1.5 V at 298 K. Charge conditions (2nd cycle): a constant current of 450 mA g^{-1} until a voltage of 0.005 V and a constant voltage of 0.005 V until a current of 15 mA g^{-1}. Charge conditions (after 3rd cycle): a constant current of 750 mA g^{-1} until a voltage of 0.005 V and a constant voltage of 0.005 V until a current of 15 mA g^{-1}. Discharge conditions (2nd cycle): a constant current of 450 mA g^{-1} until a voltage of 1.5 V. Discharge conditions (after 3rd cycle): a constant current of 750 mA g^{-1} until a voltage of 1.5 V.

Table and figure captions

Table 1 Representative reports on battery and electrode characteristics of the SiO negative electrode.

Table 2 Thermodynamic data for the Li–Si–O system at 298 K used for the calculation.

Table 3 Equilibrium phases and electrode potentials during the Li insertion reaction for a SiO negative electrode at 298 K.

Table 4 The calculated reactions for the Li insertion of a SiO negative electrode at 298 K.

Table 5 The calculated reactions for the Li extraction of a SiO negative electrode at 298 K.

Table 6 Charge and discharge capacities and coulombic efficiency for the 1st cycle of SiO/EC:DEC(1:1) + 1 mol L^{-1} $LiPF_6$/Li cells in the voltage range of 0.005–1.5 V at 298 K.

Fig. 1 (a) Calculated ternary phase diagram for the Li–Si–O system at 298 K. (b) Transition of formed phases during the Li insertion for a SiO negative electrode at 298 K shown in the ternary phase diagram for Li–Si–O system.

Fig. 2 Reaction pathway during (a) the Li insertion for a SiO_2 negative electrode and (b) the Li extraction for a Li_4SiO_4 electrode at 298 K shown in the ternary phase diagram for Li–Si–O system.

Fig. 3 Transition of equilibrium electrode potential during the Li (a) insertion and (b) extraction after the formation of $Li_{13}Si_4$ for a SiO negative electrode at 298 K shown in the ternary phase diagram for Li–Si–O system.

Fig. 4 (a, b) TEM images and (c) XRD patterns for the silicon monoxide particles before and after the heat treatment in an Ar atmosphere at 1273 K and 1473 K.

Fig. 5 (a) Charge and discharge curves for the 1st cycle of SiO/EC:DEC(1:1) + 1 mol L^{-1} $LiPF_6$/Li cells in the voltage range of 0–1.5 V at 298 K. Charge conditions: a constant current of 15 mA g^{-1} until a voltage of 0 V. Discharge conditions: a constant current of 15 mA g^{-1} until a voltage of 1.5 V. (b) Charge and discharge curves for the 1st cycle of KB+PI/EC:DEC(1:1) + 1 mol L^{-1} $LiPF_6$/Li cells in the voltage range of 0–1.5 V at 298 K. Charge conditions: a constant current of 10 mA g^{-1} until a voltage of 0 V. Discharge conditions: a constant current of 10 mA g^{-1} until a voltage of 1.5 V.

Fig. 6 (a) Charge and (b) discharge curves for the 1st cycle of SiO/EC:DEC(1:1) + 1 mol L^{-1} $LiPF_6$/Li cells in the voltage range of 0.005–1.5 V at 298 K. Charge conditions: a constant current of 150 mA g^{-1} until a voltage of 0.005 V, and a constant voltage of 0.005 V until a current of 15 mA g^{-1}. Discharge conditions: a constant current of 150 mA g^{-1} until a voltage of 1.5 V.

Fig. 7 Comparison of transition of formed phases during the Li insertion for (a) amorphous and (b) disproportionated SiO negative electrodes at 298 K.

Fig. 8 Charge and discharge curves for the (a) 2nd and (b) 10th cycles of SiO/EC:DEC(1:1) + 1 mol L^{-1} $LiPF_6$/Li cells in the voltage range of 0.005–1.5 V at 298 K. Charge conditions (2nd cycle): a constant current of 450 mA g^{-1} until a voltage of 0.005 V, and a constant voltage of 0.005 V until a current of 15 mA g^{-1}. Charge conditions (after 3rd cycle): a constant current of 750 mA g^{-1} until a voltage of 0.005 V, and a constant voltage of 0.005 V until a current of 15 mA g^{-1}. Discharge conditions (2nd cycle): a constant current of 450 mA g^{-1} until a voltage of 1.5 V. Discharge conditions (after 3rd cycle): a constant current of 750 mA g^{-1} until a voltage of 1.5 V.